Response to Reviewer 1

Reviewer comments are quoted in italics, and our responses follow in regular font. After each response, we quote the new or changed text of the revised manuscript and Supplement. Line numbers in our responses refer to the revised manuscript with tracked changes; line numbers in the reviewer's comments refer to the initial submission.

> *The authors demonstrated that stratospheric aerosol injections using purely scattering particles can produce positive shortwave radiative forcing over high-albedo surfaces at low solar zenith angles. The authors perform radiative transfer simulations using libRadtran (discrete-ordinate method) and the two-stream approximation.*
>
> *Overall, I think it is an interesting and timely study that fits the scope of ACP. I suggest minor revisions.*
>
> *Below are some general and specific comments intended to improve the manuscript.*

We thank the reviewer for the careful and constructive review, which helped us improve the manuscript. In response to the general comments, we added a convergence test for the number of DISORT streams (General Comment 1), a sensitivity study for the particle size distribution (General Comment 2), the reviewer's independent check of R↑ (General Comment 4), sensitivity tests for prescribed non-Lambertian surface reflection (General Comment 5), an assessment of polarization (General Comment 6), and a test of the plane-parallel geometry with pseudo-spherical DISORT and a Monte Carlo calculation (General Comment 7). The revised manuscript also states the assumed particle shape and discusses its effect (General Comment 3). These calculations are presented in five new sections of the Supplement (Sects. S3–S7).

While preparing this response, we found that some submitted figures had been produced with model settings from an earlier stage of the work. We regenerated these figures with the settings stated in Sect. 2 and corrected the affected numbers, as described under "Author-initiated corrections" at the end of this document.

General comments

General Comment 1

> *Why is the number of ordinates 16 (discrete ordinates method)? It would be good to explain this in the manuscript. The DISORT accuracy depends critically on the number of discrete ordinates, particularly for phase functions with a pronounced forward peak. Furthermore, the relationship to Legendre moment truncation (here nnom = 17) is crucial. In DISORT, the number of Legendre moments of the phase function expansion must correspond at least to the number of streams/ the number of ordinates. With 16 streams and 17 moments, the minimum requirement is met only just, with a buffer of one moment. Was a delta-M scaling*

used to correctly cover the forward peak of the phase function despite the small number of moments? 17 = 16 + 1 is a limit that is just accepted by DISORT, but is it also based on a convergence analysis (with nnom = 17, 32, 64, . . .) to ensure that the phase function resolution is not an additional factor (for ϕ values)?

Our convergence tests support the use of 16 streams for this study. We also corrected the number of Legendre moments stated in the manuscript.

(1) The expansion supplied to DISORT contained 33 Legendre moments (l = 0–32), not 17. The value 17 belonged to a different libRadtran input option ("disort_intcor moments"), which selects the intensity correction method and does not affect irradiances.

(2) DISORT used delta-M scaling in all calculations (Wiscombe, 1977). A 16-stream irradiance calculation then uses only the first 17 moments. Truncating the input to exactly 17 moments gave the same irradiances as the 33-moment input to the last output digit. We therefore tested convergence by increasing the number of streams.

(3) Increasing the number of streams from 16 to 32 changes Φ by at most 0.13 %, and increasing it further from 32 to 64 changes Φ by at most 0.03 %. The ADRF changes by less than 0.01 W m^{-2}. These changes are much smaller than the difference between DISORT and RODENTS (Φ = 3.16 vs. 2.01 at SZA = 5°), which supports the use of 16 streams for this study.

Revised manuscript, lines 131–140:

The scattering phase function was expanded in Legendre polynomials to provide the angular scattering representation required by DISORT. The expansion supplied to the solver contained 33 moments (l = 0–32), with Legendre coefficients computed following the pmom algorithm of libRadtran (Emde et al., 2016). Over all scattering angles, the largest relative difference between the phase function reconstructed from these moments and the Mie phase function is 3.6 % at the shortest wavelength (250 nm) and below 0.01 % at 550 nm (Sect. S1). DISORT applies delta-M scaling (Wiscombe, 1977) by treating the narrow forward-scattering peak of the phase function as unscattered light. A 16-stream irradiance calculation then depends only on the first 17 moments. Calculations with 16, 32 and 64 streams differ by less than 0.15 % in Φ and by less than 0.01 W m^{-2} in the ADRF (Sect. S3). Details of the Legendre polynomial fitting procedure, including the normalization condition, recurrence relation, and numerical quadrature method, are provided in Sect. S1 of the Supplement.

Revised Supplement, Sect. S1, text after Eq. (S3):

for l = 0, 1, . . ., 32, where N = 90 and nmom = 33. The Legendre polynomials

Revised Supplement, Sect. S1, text after Eq. (S4):

starting from $P_0(\mu) = 1$ and $P_1(\mu) = \mu$. These moments were computed following the pmom function from libRadtran and written into the aerosol input file in the format required by libRadtran. Across all scattering angles, the largest relative difference between the phase function reconstructed from the 33 moments and the Mie phase function is 3.6 % at 250 nm, the shortest wavelength considered, and below 0.01 % at 550 nm.

Revised Supplement, new Sect. S3:

S3 Convergence with the number of DISORT streams

The phase-function expansion supplied to DISORT contained 33 Legendre moments (l = 0–32). DISORT applies delta-M scaling (Wiscombe, 1977), so a calculation with N streams uses only the first N + 1 moments. Higher-order moments do not change the computed irradiances. Convergence must therefore be tested by varying the number of streams. We computed a second set of 129 moments using Gauss–Legendre quadrature of the Mie phase function. Its first 33 moments differ from those used in the main text, which were computed with the trapezoidal rule (Sect. S1). The differences are less than 7×10^{-3}. Using this set, we repeated the broadband calculations for surface albedos of 0–0.9, with 16 and 32 streams at SZA = 5–85° and with 64 streams at SZA = 5°, 25°, 45°, 65° and 85°.

Increasing the number of streams from 16 to 32 changes the reflectance asymmetry parameter Φ by at most 0.13 %. Increasing it from 32 to 64 changes this parameter by at most 0.03 %. For each pair of calculations, we compared the instantaneous ADRF at every combination of SZA and surface albedo represented in both calculations. The largest difference is 0.008 W m^{-2} between 16 and 32 streams and 0.001 W m^{-2} between 32 and 64 streams (Table S1). The SZA at which Φ = 1 shifts by 0.03° between 16 and 64 streams. With 16 streams, replacing the 33 moments of the main text with the 129-moment set changes Φ by at most 0.03 %. Because a 16-stream calculation uses only the first 17 moments, this small change comes from differences between the first 17 moments of the two sets, rather than from the additional moments. The 16-stream configuration used in the main text is therefore sufficient for the analysis presented in this study (Fig. S4, Table S1).

Table S1. Convergence of the DISORT calculations with the number of streams (Sect. S3). The table gives the largest changes over SZA = 5–85° (for 32 → 64 streams, at SZA = 5°, 25°, 45°, 65° and 85°) and surface albedos of 0–0.9 for the purely scattering alumina layer (250–3000 nm). F↑ is the upward irradiance at the TOA.

Comparison	**max |ΔΦ/Φ|**	**max |ΔF↑/F↑|**	**max |ΔADRF|**
33 vs. 129 moments (both 16 streams)	0.03 %	0.09 %	–
16 → 32 streams	0.13 %	0.023 %	0.008 W m^{-2}
32 → 64 streams	0.03 %	0.0002 %	0.001 W m^{-2}

Revised Supplement, Fig. S4 and its caption:

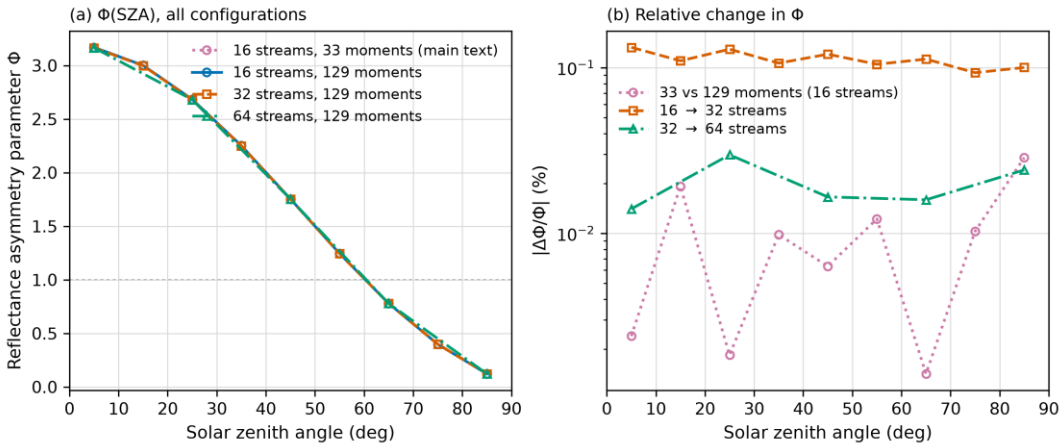


Figure S4. Convergence with the number of streams. Panel (a) shows Φ(SZA) computed with 16 streams and the 33 moments used in the main text, and with 16, 32 and 64 streams and the 129-moment set (64 streams only at SZA = 5°, 25°, 45°, 65° and 85°). The four curves coincide. Panel (b) shows the relative change in Φ between these calculations; all changes are below 0.15 %.

General Comment 2

All results rely on a single particle size distribution. Since the authors explicitly generalise to "any optically thin scattering layer" (Abstract, l. 21) and specifically to reentry-derived alumina, whose PSD likely differs from the SAI-optimised configuration used here, a sensitivity analysis across particle size would be valuable to confirm that the quantitative results are not strongly dependent on the chosen PSD. At minimum, the transferability to other PSD should be discussed.

We added a sensitivity study with three size distributions in addition to the baseline (median diameter D_g = 430 nm and geometric standard deviation σ_g = 1.5): D_g = 215 nm and 860 nm at σ_g = 1.5, and D_g = 430 nm at σ_g = 1.8. Together, the four distributions span a factor of four in median diameter. The magnitudes of Φ and the ADRF depend on the size distribution. For all distributions, however, Φ is well above 1 at small SZA, the Φ = 1 crossover stays within 2° of 60°, and the difference between DISORT and RODENTS remains. The revised Sect. 4.3 explains why these results hold for other size distributions. For an optically thin layer and at a given wavelength, Φ depends on particle size and composition only through the phase function (new Eqs. 13–15). When the phase function is approximated by its first two Legendre terms, Φ = 1 at SZA = 60° for any size distribution.

The size distribution of reentry-derived alumina is not well constrained by observations. Maloney et al. (2025) assumed initial emission radii of 10 nm and 100 nm, corresponding to diameters of 20 nm and 200 nm. Our smallest test distribution has a median diameter of 215 nm, close to the larger of these initial diameters; this comparison does not imply that the size distributions after atmospheric evolution are similar. For particles much smaller than the wavelength, the phase

function is symmetric about 90°, so Eq. (15) gives $\Phi = 2\mu_0$, again with $\Phi = 1$ at 60°, although the forcing per unit mass becomes small.

Revised manuscript, lines 99–101:

> The forcing magnitudes reported here apply to this size distribution. All size distributions tested in Sect. S6 produce positive forcing over sufficiently bright surfaces at small SZA, and the difference between DISORT and RODENTS persists.

Revised manuscript, lines 336–356:

> For an optically thin layer, in which most photons are scattered at most once, Φ can be written in closed form. In this derivation, $\mu_0 = \cos\theta$ is the direction cosine of the solar beam (written μ in Eqs. 4–12), and μ is the direction cosine of any other direction. For light arriving at direction cosine μ, let β(μ) be the fraction of the light scattered by the particles that travels back toward the side from which it came (upward for sunlight from above, downward for light from the surface). A collimated beam at μ_0 crosses the layer along the slant optical depth τ/μ_0, where τ is the vertical optical depth of the layer. The fraction $\omega\tau/\mu_0$ of the beam is scattered, where ω is the single-scattering albedo. The reflectance of the layer for the direct beam is therefore
>
> $$R_{\downarrow}(\mu_0) = \frac{\omega\tau\beta(\mu_0)}{\mu_0} \qquad (13)$$
>
> Light reflected by a Lambertian surface reaches the bottom of the aerosol layer from all directions in the upward hemisphere. The directions between μ and μ + dμ carry the fraction 2μ dμ of the upward flux. Because the layer is vertically uniform, it reflects light from below in the same way as light from above. Light arriving from direction μ is therefore reflected with R↓(μ). Integrating over all upward directions gives
>
> $$R_{\uparrow} = 2\int_0^1 R_{\downarrow}(\mu)\mu \mathrm{d}\mu = 2\omega\tau\bar{\beta}, \text{ with } \bar{\beta} = \int_0^1 \beta(\mu)\mathrm{d}\mu \qquad (14)$$
>
> Dividing Eq. (14) by Eq. (13) gives
>
> $$\Phi = \frac{R_{\uparrow}}{R_{\downarrow}} = \frac{2\mu_0\bar{\beta}}{\beta(\mu_0)} \qquad (15)$$
>
> Equations (13)–(15) are leading-order results for small τ and do not hold for directions near the horizon with $\mu \lesssim \tau$; the radiative transfer simulations include these directions. At a given wavelength, the optical depth and the single-scattering albedo cancel in Eq. (15). Particle size and composition therefore affect Φ only through the phase function. When the phase function is approximated by its first two Legendre terms, the backscattered fraction is $\beta(\mu) = \frac{1}{2} - \frac{3}{4}g\mu$, where g is the asymmetry parameter. Because β(μ) is linear in μ, its average $\bar{\beta}$ equals its value at $\mu = \frac{1}{2}$. It follows from Eq. (15) that $\Phi = 1$ at $\mu_0 = \frac{1}{2}$, i.e., at SZA = 60°, for any g. Higher-order Legendre terms and effects beyond first order in τ change this result. For the size distributions examined in Sect. S6, the simulated crossover lies within 2° of 60°.

Revised manuscript, lines 438–441:

> The size distribution of such particles depends on their source. Across the size distributions of Sect. S6, which span a factor of four in median diameter and include a broader distribution, Φ at SZA = 5° differs from its baseline value by less than 18 %. The Φ = 1

crossover stays within 58–61°, close to the 60° obtained from Eq. (15) with the first two Legendre terms of the phase function.

Revised manuscript, lines 468–472:

Shape and size are less certain for reentry-derived particles. Reentry metals have been observed within stratospheric sulfate particles (Murphy et al., 2023). Maloney et al. (2025) assumed initial alumina emission radii of 10 nm and 100 nm, and Ferreira et al. (2024) examined the formation of nanometer-scale alumina particles during reentry. These studies do not establish the size and shape of the particles after their subsequent atmospheric evolution. The homogeneous-sphere calculation is therefore an idealization for this source.

Revised Supplement, new Sect. S6:

S6 Sensitivity to the particle size distribution

All results in the main text use a single lognormal size distribution (median diameter D_g = 430 nm, geometric standard deviation σ_g = 1.5; Sect. 2.1). This section tests how the reflectance asymmetry depends on this choice. For an optically thin layer, $\Phi = 2\mu_0\bar{\beta}/\beta(\mu_0)$ (Eq. 15 of the main text). Here, $\beta(\mu)$ is the fraction of scattered light that returns toward the side from which it came when the light arrives at direction cosine μ, and $\bar{\beta}$ is the average of $\beta(\mu)$ over μ. At a given wavelength, the optical depth and the single-scattering albedo cancel in Eq. (15), so the size distribution affects Φ only through the phase function. When the phase function is approximated by its first two Legendre terms, Φ = 1 at SZA = 60° for any asymmetry parameter (Sect. 4.3).

We repeated the Mie calculations of Sect. 2.2 for three additional size distributions: median diameters of 215 nm and 860 nm (half and twice the baseline value) at σ_g = 1.5, and a broader distribution with σ_g = 1.8 at the baseline median diameter of 430 nm. Together with the baseline, these distributions span a factor of four in median diameter. Optical properties recomputed for the baseline distribution agree with those of the main text to better than 7×10^{-3} in every Legendre moment. For each distribution, we computed $R\downarrow(\mu)$ at $A_s = 0$ (Eq. 10) using DISORT (16 streams) at the quadrature points of Sect. S4 and at the nine SZA values of the main text. We then obtained $R\uparrow$ from the integral $R\uparrow = 2\int_0^1 R\downarrow(\mu)\mu\, d\mu$, which agrees with the inversion of Eq. (11) to within 0.06 % for the baseline distribution (Sect. S4). For RODENTS, the integral does not give the two-stream $R\uparrow$ (Sect. S4). We therefore obtained $R\uparrow$ by inverting Eq. (11) using the simulations for A_s between 0.3 and 0.95. The 860 nm distribution has the most forward-peaked phase function and is therefore the most demanding case for the number of streams. We repeated the DISORT calculations for this distribution with 32 streams; Φ changes by at most 0.11 %.

Table S4 and Fig. S7 summarize the results. Across the four distributions, $\langle\tau\rangle$, the optical depth of the layer averaged over 250–3000 nm and weighted by the incident solar spectral irradiance, changes by a factor of about 26. The asymmetry parameter at 550 nm changes from 0.54 to 0.57. Φ at SZA = 5° ranges from 2.60 to 3.66 (3.16 for the baseline), and the DISORT Φ = 1 crossover lies between 58.2° and 61.1°, i.e., within 2° of 60°. When the leading-order expression of Eq. (15) is evaluated with the full phase function of each distribution, the crossover lies at 61.3–62.1°. The full radiative transfer calculations shift the crossover to smaller SZA. At SZA = 5°, Φ from the full calculations is lower than the

leading-order value by 3 % for the thinnest layer ($\langle\tau\rangle$ = 0.006, 215 nm) and by 22 % for the thickest ($\langle\tau\rangle$ = 0.154, 860 nm). These differences include all effects beyond first order in τ, such as the attenuation of the beam within the layer and multiple scattering. The RODENTS crossover lies at 48.4° for all four distributions. This value follows from the two-stream equations: for a thin layer, the δ-Eddington two-stream method used by RODENTS gives $\Phi_{2s} = 3\mu_0(1 - g')/(2 - 3g'\mu_0)$, with $g' = g/(1 + g)$, so that $\Phi_{2s} = 1$ at $\mu_0 = 2/3$ (SZA = 48.2°) for any g. The simulated value of 48.4° results from linear interpolation in μ_0 between the simulated SZA values of 45° and 55°. The magnitude of the ADRF scales with the optical depth of the layer and therefore depends on the size distribution. All four distributions produce positive forcing over sufficiently bright surfaces at small SZA, and the difference between the two solvers persists.

Table S4. Sensitivity of the reflectance asymmetry to the particle size distribution (purely scattering alumina, 250–3000 nm). For DISORT, R↑ is computed using the integral of Sect. S4; for RODENTS, it is computed by inverting Eq. (11). The crossover SZA is interpolated linearly in μ_0 between the nine SZA values of the main text. $\langle\tau\rangle$ is the optical depth of the layer averaged over 250–3000 nm and weighted by the incident solar spectral irradiance.

Size distribution (D_g, σ_g)	**g (550 nm)**	**$\langle\tau\rangle$**	**Φ (SZA = 5°), DISORT**	**Φ = 1 crossover, DISORT**	**Φ (SZA = 5°), RODENTS**	**Φ = 1 crossover, RODENTS**
430 nm, 1.5 (baseline)	0.537	0.0377	3.16	60.4°	2.01	48.4°
215 nm, 1.5	0.551	0.0059	3.66	61.1°	2.01	48.4°
860 nm, 1.5	0.573	0.1536	2.60	58.2°	1.96	48.4°
430 nm, 1.8	0.552	0.0536	3.01	60.1°	2.02	48.4°

Revised Supplement, Fig. S7 and its caption:

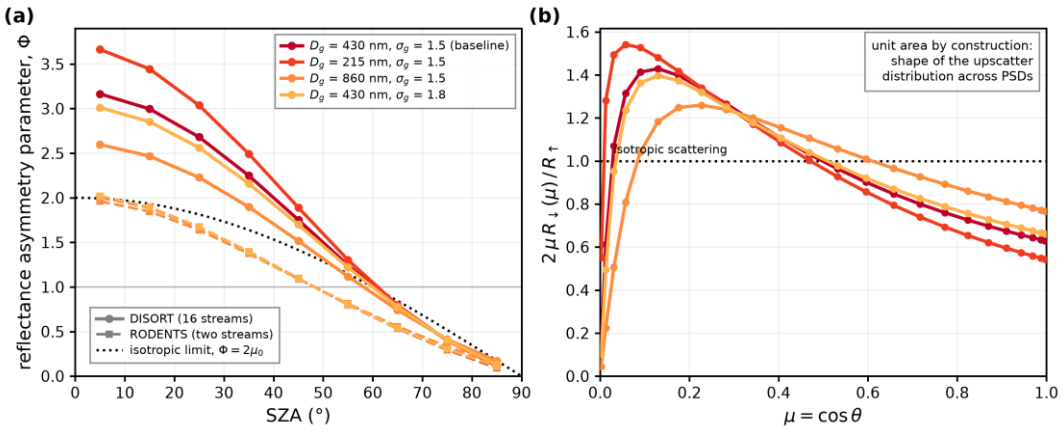


Figure S7. Sensitivity of the reflectance asymmetry to the particle size distribution. Panel (a) shows Φ(SZA) for the four size distributions of Table S4, computed with DISORT (16 streams, solid) and RODENTS (dashed). The dotted curve is $\Phi = 2\mu_0$, the result of Eq. (15) for a phase function that is symmetric about 90° (β = ½). Panel (b) shows the normalized flux-weighted reflectance 2μR↓(μ)/R↑ (DISORT), which equals β(μ)/β̄ for an optically thin layer.

General Comment 3

What is the assumed particle shape of the alumina particles (spherical, fractal aggregates, ...). Please explain. Furthermore, it should be discussed whether the assumed shape of the particles has an impact on the results.

We model the particles as homogeneous spheres, which serve as a reference particle shape, and compute their optical properties with Lorenz–Mie theory. The revised Sect. 2.2 states this assumption and its limitations. Model simulations of alumina injection find that coagulation into non-spherical aggregates is minor for injected particle radii larger than about 200 nm under the conditions examined (Weisenstein et al., 2015; Vattioni et al., 2024). This is comparable to the median radius of our baseline distribution (215 nm; median diameter 430 nm). These simulations do not establish that aggregation is negligible in concentrated injection plumes. Spherical alumina particles have also been collected in the stratosphere and attributed to solid-rocket exhaust (Brownlee et al., 1976), although those particles (3–8 μm) were larger than ours.

The revised Conclusions discuss the effect of shape. Non-spherical particles, such as the irregular-shaped commercial alumina powders measured by Kapoor et al. (2026), have phase functions that differ from those of spheres, which can change Φ and the forcing. For the dust-like spheroids examined by Mishchenko et al. (1997), the asymmetry parameter and the backscattered fraction differ from those of equivalent spheres by less than about 10 % in most cases, but this result was obtained for mineral dust and does not provide an error bound for alumina. When the phase function is approximated by its first two Legendre terms, the $\Phi = 1$ crossover lies at SZA = 60° for any asymmetry parameter (Eq. 15). Quantifying the effect for non-spherical alumina would require T-matrix or discrete-dipole calculations for representative particle shapes, which are beyond the scope of this study.

Revised manuscript, lines 120–130:

> We computed the aerosol optical properties required as input to the RTE – extinction coefficient, SSA, and scattering phase function – using Lorenz–Mie theory for homogeneous spherical particles, as implemented in the PyMieScatt Python library (Sumlin et al., 2018). Injected solid particles may coagulate into non-spherical aggregates, depending on particle size, concentration and injection conditions. Model simulations of alumina injection find that this self-coagulation is minor for particle radii larger than about 200 nm under the conditions examined (Weisenstein et al., 2015; Vattioni et al., 2024), comparable to the median radius of the size distribution used here (215 nm; Sect. 2.1). These simulations do not establish that aggregation is negligible in concentrated injection plumes. Spherical alumina particles have also been collected in the stratosphere and attributed to solid-rocket exhaust (Brownlee et al., 1976), although these particles (3–8 μm) were larger than those considered here. The effect of particle shape is discussed in Sect. 5. Wavelength-dependent refractive indices of alumina from Tropf and Thomas (1997) were used as input, and the optical properties were calculated over the spectral range of 250 nm to 3000 nm.

Revised manuscript, lines 461–472:

> The particles are modeled as homogeneous spheres (Sect. 2.2). Non-spherical particles, such as aggregates, have phase functions that differ from those of equivalent spheres. These differences can change $\beta(\mu)$ and, through it, Φ and the forcing. For the dust-like spheroids examined by Mishchenko et al. (1997), the asymmetry parameter and the backscattered fraction differ from those of equivalent spheres by less than about 10 % in most cases. This result was obtained for mineral dust and does not provide an error bound for alumina. When the phase function is approximated by its first two Legendre terms, the $\Phi = 1$ crossover lies at SZA = 60° for any asymmetry parameter (Eq. 15). The higher-order Legendre terms depend on particle shape, and quantifying their effect for alumina requires calculations for representative non-spherical particles. Shape and size are less certain for reentry-derived particles. Reentry metals have been observed within stratospheric sulfate particles (Murphy et al., 2023). Maloney et al. (2025) assumed initial alumina emission radii of 10 nm and 100 nm, and Ferreira et al. (2024) examined the formation of nanometer-scale alumina particles during reentry. These studies do not establish the size and shape of the particles after their subsequent atmospheric evolution. The homogeneous-sphere calculation is therefore an idealization for this source.

General Comment 4

> *The R↑ values derived from Eq. 11 in the manuscript can be cross-checked using a theoretically exact, independent method. According to the classical relationships of the radiative transfer theory, R↑ should be the flux-weighted integral of R↓ (ϕ) over all angles of incidence. Since R↓ (ϕ) is already available from the DISORT simulations, would this be a method independent of the functional form of the adding model? Perhaps I have missed an obvious point.*

We thank the reviewer for this suggestion and have implemented the independent check. The relation $R\uparrow = 2\int_0^1 R\downarrow(\mu)\mu\, d\mu$ does not use the adding model. In radiative transfer, it states that the spherical albedo of the layer is the flux-weighted average of its plane albedo (Stamnes et al., 2017). With the DISORT values of $R\downarrow(\mu)$, it gives $R\uparrow = 0.019303$, agreeing with the value of 0.019291 from Eq. (11) to within 0.06 %. R↑, and therefore Φ, is thus not an artifact of the adding model. For RODENTS, the integral (0.01813) is 43 % larger than the R↑ extracted from its simulations (0.01270). This difference shows that the two-stream underestimate of Φ comes mainly from the layer's reflectance for diffuse light from the surface rather than from its reflectance for the direct beam.

Revised manuscript, lines 389–401:

> The value of R↑ can be checked without the adding model. The first equality in Eq. (14), $R\uparrow = 2\int_0^1 R\downarrow(\mu)\mu\, d\mu$, holds for any layer that reflects light from below in the same way as light from above. It is not restricted to thin layers. In radiative transfer, a layer's reflectance for isotropic illumination is called its spherical albedo. This is the flux-weighted average of its reflectance for a collimated beam (its plane albedo; e.g., Stamnes et al., 2017). We evaluated this integral using DISORT values of $R\downarrow(\mu)$ computed at $A_s = 0$, with the quadrature described in Sect. S4. The result, $R\uparrow = 0.0193$, agrees to within 0.1 % with the value 0.0193 obtained by inverting the adding model (Eq. 11) with the simulations for A_s

between 0.3 and 0.95 (Sect. S4, Fig. S5, Table S2). R↑, and therefore Φ, is not an artifact of the inversion. For RODENTS, the same integral gives 0.0181, whereas the R↑ extracted from the RODENTS simulations is 0.0127, so the integral is 43 % larger. This difference is expected for the δ-Eddington two-stream method of RODENTS, which describes diffuse light by a single effective direction, so its reflectance for diffuse light is not the average of its reflectance for collimated beams over all directions. The comparison also shows where most of the two-stream underestimate of Φ (Fig. 4a) comes from. The integral of the RODENTS values of R↓(μ) is only about 6 % below the DISORT value, so RODENTS reflects the collimated beam nearly correctly. Its main error lies in the reflectance for diffuse light from the surface.

Revised Supplement, new Sect. S4:

S4 Independent check of R↑

R↑, the reflectance of the layer for light reflected by the surface, can be computed without the adding model of Sect. 4. For a layer that reflects light from below in the same way as light from above, $R\uparrow = 2\int_0^1 R\downarrow(\mu)\mu\, d\mu$ (Eq. 14 of the main text), where R↓(μ) is the reflectance of the layer for a collimated beam. In radiative transfer terms, R↑ is the spherical albedo of the layer and R↓(μ) its plane albedo (e.g., Stamnes et al., 2017). The relation does not depend on the optical depth or the phase function of the layer. The symmetry condition holds here because the aerosol extinction is uniform over 18–24 km and the main simulations contain no molecular scattering or absorption.

We computed $R\downarrow(\mu) = E(A_s = 0, \mu)/S(\mu)$ (Eq. 10) using both solvers and the configuration of the main text (Mie optical properties, 250–3000 nm, DISORT with 16 streams, and RODENTS). We evaluated the integral using a 24-point Gauss–Legendre quadrature in $\mu \in (0, 1)$; using 12 points instead changes the DISORT integral by only 0.02 %. For DISORT, the integral gives R↑ = 0.019303, which agrees with the value of 0.019291 obtained by inverting the adding model (Eq. 11) to within 0.06 % (Table S2, Fig. S5). For RODENTS, the integral (0.01813) is only about 6 % below the DISORT value, so RODENTS reflects the collimated beam nearly correctly. It is, however, 43 % larger than the R↑ obtained by inverting the RODENTS simulations (0.01270). The two-stream underestimate of Φ (Fig. 4a) therefore comes mainly from the RODENTS reflectance for diffuse light from the surface, which is 30 % below the integral of its own R↓(μ).

Table S2. Independent check of R↑. The integral is evaluated using R↓(μ) at the 24 Gauss–Legendre points (Fig. S5). The value from Eq. (11) is the mean over the SZA grid of R↑ extracted from the simulations with A_s between 0.3 and 0.95 (Fig. S3).

Solver	**$R\uparrow = 2\int_0^1 R\downarrow(\mu)\mu\, d\mu$**	**R↑ from Eq. (11)**	**Difference**
DISORT (16 streams)	0.019303	0.019291	+0.06 %
RODENTS (two streams)	0.01813	0.01270	+43 %

Revised Supplement, Fig. S5 and its caption:

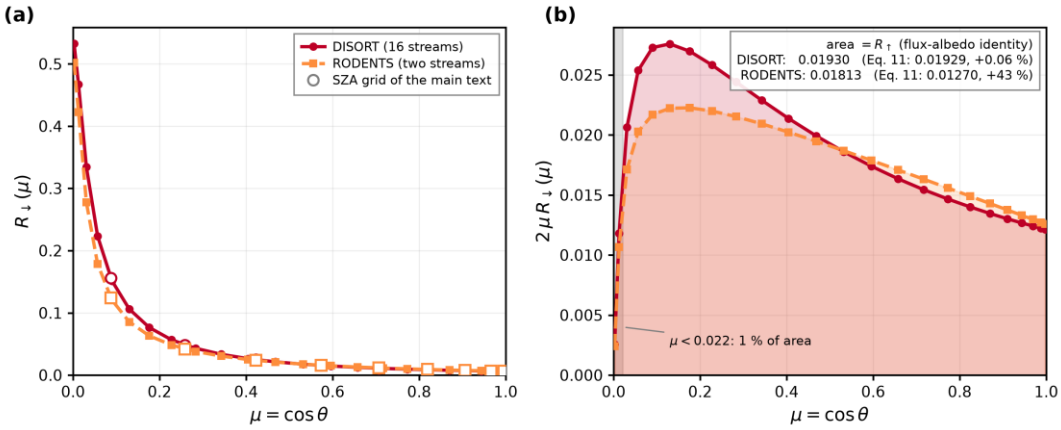


Figure S5. Independent check of R↑. Panel (a) shows the reflectance of the layer for a collimated beam, R↓(μ), computed at $A_s = 0$ at the 24 Gauss–Legendre points in $\mu = \cos\theta$ (filled symbols) for DISORT (16 streams) and RODENTS. Open symbols mark the SZA values of the main text, at which the recalculated R↓(μ) agrees with the original simulations to better than 0.05 %. Panel (b) shows the integrand 2μR↓(μ). The shaded area equals R↑, the reflectance of the layer for light from a Lambertian surface. For DISORT, the area agrees with R↑ from Eq. (11) to within 0.06 %; for RODENTS, it exceeds the two-stream R↑ by 43 % (Sect. S4). The gray band marks $\mu < 0.022$, the directions for which the plane-parallel path through the layer is longer than the longest path from the bottom to the top of the curved layer (277 km). These directions contribute 1 % of the area. On the curved Earth, the ground cannot illuminate the layer from the wider range $\mu < 0.075$ (Sect. S5).

General Comment 5

L. 347 - 349: Non-Lambertian effects are already being discussed here in relation to clouds. Does the same limitation apply to snow and ice? Particularly for small solar zenith angles, and especially where fresh snow exhibits a pronounced forward peak?

Yes, the same limitation applies to snow and ice, and the revised manuscript now discusses it. Field measurements show that the forward peak of snow reflectance is pronounced mainly at large SZA and at wavelengths where ice absorbs more strongly (Warren, 1982; Hudson et al., 2006). At visible wavelengths, with the sun near the zenith, laboratory measurements show that snow reflects almost equally in all directions, with slightly lower radiance toward the horizon (Dumont et al., 2010).

We added Eq. (S12), which weights the layer reflectance R↓(μ) by the angular distribution of radiance leaving the surface, and Eq. (S13), which defines two prescribed sensitivity profiles. In both, the radiance toward the horizon is 1 + b times the vertical radiance; in the first profile, the change spreads over the whole upward hemisphere, and in the second, it is confined to directions near the horizon. These profiles are sensitivity tests and are not fitted to snow measurements. A horizon radiance 20 % higher or lower than the vertical radiance changes Φ by less than 5 %, and a factor of two changes Φ by less than 18 %. For a given profile, the relative change in Φ is the same at every SZA. A profile with slightly less radiance toward the horizon, as measured for

snow when the sun is near the zenith, lowers Φ relative to a Lambertian surface. Applying these results quantitatively to snow would require its SZA- and wavelength-dependent reflected radiance, obtained from an appropriate surface BRDF.

Revised manuscript, lines 90–92:

> We examine the plane-parallel assumption in Sects. 4.2 and 5 and in Sect. S5 of the Supplement, and the Lambertian-surface assumption in Sect. 5 and in Sect. S7 of the Supplement.

Revised manuscript, lines 480–491:

> Snow and ice surfaces also depart from the Lambertian assumption. Field measurements at SZA between 52° and 87° show that snow appears brightest when viewed near the horizon toward the sun. This effect changes little with SZA below about 60° and grows at larger SZA and at wavelengths where ice absorbs more strongly (Warren, 1982; Hudson et al., 2006). At visible wavelengths, which carry most of the sunlight reflected by snow, laboratory measurements show that snow reflects almost equally in all directions when the sun is near the zenith, with slightly less light toward the horizon (Dumont et al., 2010). We tested how sensitive Φ is to such departures from a Lambertian surface, using two prescribed angular profiles of the radiance leaving the surface (Sect. S7). For these profiles, a radiance in near-horizontal directions that is 20 % higher or lower than in the vertical direction changes Φ by less than 5 %, and a factor of two changes Φ by less than 18 %. For a given profile, the relative change in Φ equals that in R↑ and is therefore the same at every SZA. For real snow, however, the angular profile itself changes with SZA, wavelength and snow properties, so these tests do not provide a general correction. A profile with slightly less radiance toward the horizon, as measured for snow when the sun is near the zenith, lowers Φ relative to a Lambertian surface.

Revised Supplement, new Sect. S7:

> **S7 Sensitivity to non-Lambertian surface reflection**
>
> The simulations assume a Lambertian surface, which sends the same radiance into all directions, whereas real snow and ice do not. Field measurements at SZA between 52° and 87° show that snow looks brightest when it is viewed near the horizon in the direction of the sun. This effect changes little with SZA below about 60° and grows at larger SZA and at wavelengths where ice absorbs more strongly (Warren, 1982; Hudson et al., 2006). At visible wavelengths, laboratory measurements show that the radiance reflected by snow changes little with viewing angle except near the horizon, where it decreases. They also show that snow reflects almost equally in all directions when the sun is near the zenith (Dumont et al., 2010). This section tests how sensitive Φ is to such departures from a Lambertian surface.
>
> If the surface sends radiance I(μ) into the direction with cosine μ, the reflectance of the layer for this light is the average of R↓(μ) weighted by the flux carried in each direction:
>
> $$R_{\uparrow}[I] = \frac{\int_0^1 I(\mu) R_{\downarrow}(\mu) \mu \mathrm{d}\mu}{\int_0^1 I(\mu) \mu \mathrm{d}\mu} \qquad \text{(S12)}$$

For a Lambertian surface, I(μ) is constant, and Eq. (S12) reduces to the integral of Sect. S4. R↓ is a property of the layer alone and does not depend on the surface, so a relative change in R↑ produces the same relative change in Φ = R↑/R↓. For a prescribed I(μ), this relative change is the same at every SZA, because R↑ does not depend on the solar beam. For real snow, I(μ) itself varies with SZA and wavelength. The flux reflected by a horizontally uniform layer depends only on the zenith angles of the incident light, not on its azimuths. Only the azimuthal average of the radiance therefore enters Eq. (S12).

In Eq. (S12), μ is the cosine of the angle between the direction of the light and the upward vertical, so μ = 1 corresponds to the vertical direction and μ = 0 to the horizon. To test how a departure from a constant radiance affects R↑, we prescribed

$$I(\mu) = I(1)[1 + bf(\mu)], \text{ with } f(1) = 0 \text{ and } f(0) = 1 \qquad \text{(S13)}$$

The factor I(1) cancels in Eq. (S12), so R↑ depends on the profile only through b and f(μ). Since f(0) = 1, the radiance toward the horizon is I(0) = I(1)(1 + b), and b = I(0)/I(1) − 1 is its relative difference from the vertical radiance I(1). The value b = 0 recovers the Lambertian surface, and b = 0.2 and b = −0.2 give a radiance toward the horizon 20 % higher and 20 % lower, respectively, than the vertical radiance. A non-negative radiance requires b ≥ −1. The function f(μ) determines the directions over which this difference is spread. We used $f(\mu) = (1 - \mu)^n$ with n = 1 and n = 8. With n = 1, f(μ) is the only linear function that satisfies both conditions, and the radiance changes linearly with μ over the whole upward hemisphere. With n = 8, the radiance stays close to its vertical value in most directions and changes appreciably only near the horizon; at μ = 0.5, for example, f(μ) is 0.5 for n = 1 but only 1/256 for n = 8. Both profiles are sensitivity tests and are not fitted to snow measurements; the value n = 8 is only an example of a change confined to directions near the horizon.

We evaluated Eq. (S12) using the DISORT values of R↓(μ) from Sect. S4. A two-stream model such as RODENTS describes diffuse light in each hemisphere by a single flux, so it cannot represent such angular distributions. For these two profiles, a radiance toward the horizon that is 20 % higher or lower than the vertical radiance (b = ±0.2) changes R↑, and therefore Φ, by less than 5 % (Table S5). For a factor of two in either direction (b = 1 or b = −0.5), Φ changes by at most 17.3 % for n = 1 and by at most 10.5 % for n = 8. For comparison, across the size distributions of Sect. S6, Φ at SZA = 5° differs from its baseline value by less than 18 %. A surface that looks brighter toward the horizon increases R↑, and one that looks darker decreases it, because the layer reflects most strongly in near-horizontal directions, where R↓(μ) is largest.

Table S5. Relative change in R↑, equal to the relative change in Φ, when the constant radiance of a Lambertian surface is replaced by the profiles of Eq. (S13), $I(\mu) \propto 1 + b(1 - \mu)$ or $I(\mu) \propto 1 + b(1 - \mu)^8$. The ratio of the radiance leaving the surface toward the horizon to the radiance leaving it vertically upward is 1 + b. Values below 1 describe a surface that looks darker toward the horizon, and values above 1 describe a surface that looks brighter. The calculations use the DISORT values of R↓(μ) at the 24 Gauss–Legendre points of Sect. S4 (Mie optical properties, 250–3000 nm).

Radiance ratio, horizon to vertical (1 + b)	$\Delta\Phi$, $I \propto 1 + b(1 - \mu)$	$\Delta\Phi$, $I \propto 1 + b(1 - \mu)^8$
0.5	−13.8 %	−5.4 %
0.8	−4.9 %	−2.1 %
1.2	+4.3 %	+2.1 %
1.5	+9.9 %	+5.3 %
2.0	+17.3 %	+10.5 %

General Comment 6

It would be helpful to have a comment on the neglect of polarisation, as well as a brief assessment of the order of magnitude of the effect. To what extent does this affect the results.

DISORT and RODENTS are scalar solvers, so our calculations neglect polarization. For unpolarized sunlight, a scalar calculation gives the singly scattered intensity exactly, and polarization affects only the second and higher orders of scattering (Mishchenko et al., 1994; Lacis et al., 1998). The mechanism identified here is a single-scattering effect (Eqs. 13–15) and is therefore not affected. For the water clouds examined by Hansen (1971), neglecting polarization changed reflected intensities by about 1 % or less, but this result does not provide an error bound for the alumina layer. A quantitative estimate would require a vector radiative transfer calculation for the same layer, which we have not performed. The revised Sect. 5 states this limitation.

Revised manuscript, lines 492–498:

A further approximation is the neglect of polarization, because DISORT and RODENTS are scalar solvers. For unpolarized incident sunlight, a scalar calculation gives the same singly scattered intensity as a vector calculation; differences arise only from the second and higher orders of scattering (Mishchenko et al., 1994; Lacis et al., 1998). Polarization therefore does not change the single-scattering mechanism identified here (Sect. 4.3). For the water clouds examined by Hansen (1971), neglecting polarization changed reflected intensities by about 1 % or less, but this result does not provide an error bound for the alumina layer. A quantitative estimate of the effect on R↓, R↑ and Φ would require a vector radiative transfer calculation with the same aerosol and surface properties.

General Comment 7

Since the central mechanism (ϕ) explicitly relies on very oblique optical paths of the diffuse upwelling radiation within the layer, a brief comment would be helpful as to whether plane-parallel approximation remains unproblematic for these path components (near 90° local zenith angles) given the layer geometry used here (18 - 23 km). A comparison with the pseudo-spherical DISORT option in libRadtran could quantitatively substantiate this.

The plane-parallel treatment of the direct beam is adequate at SZA ≤ 85°. For diffuse light from the surface, however, the layer reflectance R↑ is about 14 % smaller in spherical geometry. We assessed these two parts of the radiation field separately because libRadtran's pseudo-spherical option corrects only the direct-beam path.

(1) For the direct beam, the pseudo-spherical option corrects the attenuation of the beam for the curvature of the atmosphere, while scattered light is still treated in plane-parallel geometry. This correction changes the ADRF over a black surface by at most 0.25 % at SZA ≤ 85°. At larger SZA, a fully spherical calculation would be needed, so we now describe the results for SZA > 85° (Fig. S2) as indicative.

(2) For diffuse light from the surface, we used a Monte Carlo calculation for the homogeneous, purely scattering layer at 18–24 km (Author-initiated correction A1), with the baseline phase function at 550 nm and the solar-spectrum-averaged optical depth $\langle\tau\rangle = 0.0377$. On the curved Earth, R↑ and therefore Φ are about 14 % smaller than in plane-parallel geometry. The ground cannot illuminate the layer along the most nearly horizontal paths, oblique paths through the curved layer are shorter, and some of the light scattered downward misses the ground. With the same plane-parallel R↓ for both geometries, Φ at SZA = 5° decreases from 2.99 to 2.56, and the Φ = 1 crossover moves from 60.4° to 56.8°, still well above the RODENTS crossover of 48.4°. The forcing therefore remains positive over sufficiently bright surfaces at small SZA, and the difference between the two solvers remains. This calculation estimates the effect of curvature on Φ; it is not a fully spherical broadband calculation. The Python code and reference output logs of this calculation are available on Zenodo (Zhang, 2026).

Revised manuscript, lines 90–92:

> We examine the plane-parallel assumption in Sects. 4.2 and 5 and in Sect. S5 of the Supplement, and the Lambertian-surface assumption in Sect. 5 and in Sect. S7 of the Supplement.

Revised manuscript, lines 288–293:

> Earth's curvature removes part of this enhancement. At the altitude of the aerosol layer, the ground horizon lies 4.3–5.0° below the local horizontal. The ground therefore cannot illuminate the layer along the most nearly horizontal paths. Light that the layer scatters downward into directions between the local horizontal and the ground horizon misses the ground. In addition, oblique paths through the curved layer are shorter than in a flat layer. A Monte Carlo calculation with the baseline phase function at 550 nm and the solar-spectrum-averaged optical depth of the layer shows that, together, these effects make R↑ about 14 % smaller than in plane-parallel geometry (Sect. S5).

Revised manuscript, lines 458–461:

> For the direct beam, the pseudo-spherical correction of the attenuation for the curvature of the atmosphere changes the ADRF over a black surface by at most 0.25 % at SZA ≤ 85°. Results for SZA > 85° (Fig. S2) are indicative only (Sect. S5). For diffuse light reflected by the surface, R↑ and therefore Φ are about 14 % smaller in spherical geometry than in the plane-parallel calculation (Sect. 4.2).

Revised Supplement, new Sect. S5:

> **S5 Validity of the plane-parallel approximation**
>
> The simulations treat the aerosol layer as a flat, horizontally uniform slab (plane-parallel geometry). The reflectance asymmetry depends on the oblique paths taken by light reflected from the surface through the layer at 18–24 km, so the curvature of the Earth could affect it.

In a flat layer of geometric thickness $\Delta z = 6$ km, a ray at direction cosine μ travels a distance $\Delta z/\mu$, which grows without bound as $\mu \to 0$. On the curved Earth, two effects limit these paths. First, at the altitude of the layer, the ground horizon lies below the local horizontal, by 4.3° at 18 km and by 5.0° at 24 km. The ground therefore cannot illuminate the layer from directions with $\mu < 0.075$ (zenith angles larger than 85.7°). Likewise, light that the layer scatters downward into directions between the local horizontal and the ground horizon misses the ground. Second, for less oblique directions, the path through the curved layer is shorter than $\Delta z/\mu$. No path from the bottom to the top of the curved layer is longer than $\sqrt{((R_E + 24\ \text{km})^2 - (R_E + 18\ \text{km})^2)} \approx 277$ km, where $R_E = 6371$ km is the radius of the Earth. These near-horizontal directions matter for R↑. Directions with $\mu < 0.075$ carry only 0.56 % of the upward flux from a Lambertian surface. In the plane-parallel Monte Carlo calculation described below, however, they contribute 7.8 % of R↑ because their reflectance R↓(μ) is on average about 14 times larger than R↑.

To quantify both effects, we computed R↑ in plane-parallel and spherical geometry using a Monte Carlo code written for this study (Zhang, 2026). A Monte Carlo calculation follows the paths of many individual photons. It draws each scattering event and each new direction at random from the probabilities given by the optical properties of the medium (Marchuk et al., 1980; Mayer, 2009). Here, each photon leaves the ground upward in a direction drawn from the Lambertian distribution. The code follows it through the layer until it returns to the ground or escapes to space. R↑ is estimated from the photons that return to the ground. Reflection by the ground is not followed because R↑ is a property of the layer alone. The layer has the same properties as in the main simulations (18–24 km, $\omega = 1$, no molecular atmosphere). The phase function is the Lorenz–Mie phase function of the baseline size distribution at 550 nm, computed with the Python package miepython, version 3.3.0 (Prahl, 2026). This package implements the same Lorenz–Mie theory as PyMieScatt, which was used for the main simulations. The optical depth is the solar-spectrum-averaged value $\langle\tau\rangle = 0.0377$ of the baseline distribution (Sect. S6).

At this optical depth, about 93 % of the photons would cross the layer without being scattered and would not contribute to R↑. To reduce statistical noise, the code therefore forces every photon's first scattering event to occur inside the layer. It multiplies the photon's statistical weight by the probability of this event, $1 - \exp(-\tau_{path})$, where τ_{path} is the optical depth along the photon's path through the layer. This technique, known as forced first collision, reduces the noise without changing the expected value of R↑. R↑ is then the sum of the statistical weights of the photons that return to the ground, divided by the number of emitted photons.

In spherical geometry, the code follows each photon through three concentric spheres: the ground (radius R_E) and the bottom and top of the layer ($R_E + 18$ km and $R_E + 24$ km). The different runs use 4×10^6 to 10^7 photons per geometry. Statistical standard errors are estimated from independent batches of 10^6 photons, as the standard deviation of the batch estimates divided by the square root of the number of batches. For the main run with 10^7 photons per geometry, the standard error of R↑ is below 0.1 % in each geometry. To compute Φ, the code also follows photons in a collimated beam from above and obtains R↓ in plane-parallel geometry at SZA steps of 1°. The plane-parallel Monte Carlo value of R↑

(0.0195) is close to the broadband DISORT value (0.0193, 250–3000 nm), and the $\Phi = 1$ crossover is 60.4° in both calculations. Because the Monte Carlo calculation combines the 550 nm phase function with the solar-spectrum-averaged optical depth, this comparison is a consistency check rather than an exact benchmark. When the radius of the Earth is increased by a factor of 10^4, the relative difference between the spherical and plane-parallel results is -0.03 ± 0.17 % (one standard error), consistent with zero.

In spherical geometry, R↑ is about 14 % smaller than in plane-parallel geometry. To separate the loss of light that misses the ground from the other effects, we repeated the spherical calculation while counting every photon that leaves the bottom of the layer as returned to the ground, including photons that pass above the horizon. This calculation retains only the effects of curvature on the illumination of the layer and the path lengths. It gives a reduction of about 10 %. Photons scattered downward by the layer that miss the ground account for an additional reduction equal to about 4 % of the plane-parallel R↑.

The pseudo-spherical calculations described below show that correcting the attenuation of the direct beam for the curvature changes R↓, the reflectance of the layer for the direct beam, by at most 0.25 % at SZA ≤ 85°; these calculations still treat scattered light in plane-parallel geometry. For the present estimate of Φ, we use the same plane-parallel R↓ for both geometries, so $\Phi = R\uparrow/R\downarrow$ decreases by the same fraction as R↑. At SZA = 5°, the Monte Carlo value of Φ decreases from 2.99 to 2.56, and the $\Phi = 1$ crossover moves from 60.4° to 56.8°. It remains well above the RODENTS crossover of 48.4°. The plane-parallel Monte Carlo value of Φ at SZA = 5° (2.99) is lower than the broadband DISORT value (3.16) because the Monte Carlo calculation, which combines the 550 nm phase function with $\langle\tau\rangle$, gives an R↓ about 7 % larger at this SZA. Both the phase function and the optical depth vary with wavelength, and this combination need not reproduce their combined effect on the broadband reflectance. The spectral difference does not affect the comparison of the two geometries, which use the same R↓.

For optical depths of 0.006–0.15 (the range of the size distributions in Sect. S6) and the phase function of the baseline distribution, the reduction in R↑ ranges from 22 % to 6 %. Near-horizontal directions contribute a larger share of R↑ when their long paths through the layer remain optically thin. Like the main simulations, the calculation contains no molecular atmosphere. In the real atmosphere, light scattered by the air partly fills the directions between the local horizontal and the ground horizon.

For the direct beam, we repeated the DISORT calculations with the pseudo-spherical option of libRadtran (Emde et al., 2016). This option computes the attenuation of the direct beam along its path through the curved atmosphere, while scattered light is still computed in plane-parallel geometry. Over a black surface ($A_s = 0$), the ADRF depends only on the reflection of the direct beam by the layer. This comparison therefore tests the treatment of the direct beam alone. At $A_s = 0$, the pseudo-spherical option changes the instantaneous ADRF by at most 0.25 % at SZA ≤ 85° (Table S3, Fig. S6b). The plane-parallel treatment of the direct beam is therefore accurate over the SZA range on which the results of the main text are based. At larger SZA, the change grows rapidly (−0.8 % at 86° and −29 % at 89°).

Over brighter surfaces, the two geometries differ much more (Fig. S6a). This difference does not measure the effect of the curvature, because the pseudo-spherical calculation fails

an energy-balance test in this configuration. Because the layer is purely scattering ($\omega = 1$), a surface with $A_s = 1$ absorbs nothing. The one-dimensional column must therefore return all incident sunlight through the top of the atmosphere, and the ADRF must vanish at $A_s = 1$. The plane-parallel calculation satisfies this energy balance at every SZA, with deviations below 10^{-4} %. The pseudo-spherical calculation does not: at $A_s = 1$, its reflected flux exceeds the incident flux by 0.02 % at SZA = 45°, 3.9 % at 83°, 8.0 % at 85° and 76 % at 89° (Table S3). At each SZA, the largest difference in ADRF between the two geometries, divided by the incident flux, equals this violation of the energy balance. The pseudo-spherical option therefore cannot serve as a reference for TOA fluxes over bright surfaces at large SZA in this configuration, and a fully spherical radiative transfer model would be needed to quantify the effect of the curvature there. The results for SZA > 85° in Fig. S2 should therefore be regarded as indicative. The quantitative conclusions of the main text rest on SZA ≤ 85°, where the pseudo-spherical option changes the ADRF over a black surface by at most 0.25 %.

Table S3. Plane-parallel and pseudo-spherical DISORT calculations (16 streams, purely scattering alumina). Column 2 gives the relative change in the instantaneous ADRF at $A_s = 0$, which measures the effect of the curved path of the direct beam alone. Column 3 gives the violation of the energy balance by the pseudo-spherical calculation at $A_s = 1$ (reflected flux divided by incident flux, minus 1). The plane-parallel calculation satisfies the energy balance to output precision. At every SZA, the largest difference in ADRF between the two calculations, divided by the incident flux, equals this value.

SZA	**Change of ADRF at $A_s = 0$ (pseudo-spherical vs. plane-parallel)**	**Violation of the energy balance by the pseudo-spherical calculation (reflected/incident − 1 at $A_s = 1$)**
45°	+0.09 %	+0.02 %
65°	+0.17 %	+0.12 %
75°	+0.24 %	+0.54 %
80°	+0.25 %	+1.61 %
83°	+0.15 %	+3.85 %
85°	−0.18 %	+7.97 %
86°	−0.78 %	+12.19 %
87°	−2.15 %	+19.73 %
88°	−6.66 %	+34.84 %
89°	−28.96 %	+76.27 %

Revised Supplement, Fig. S6 and its caption:

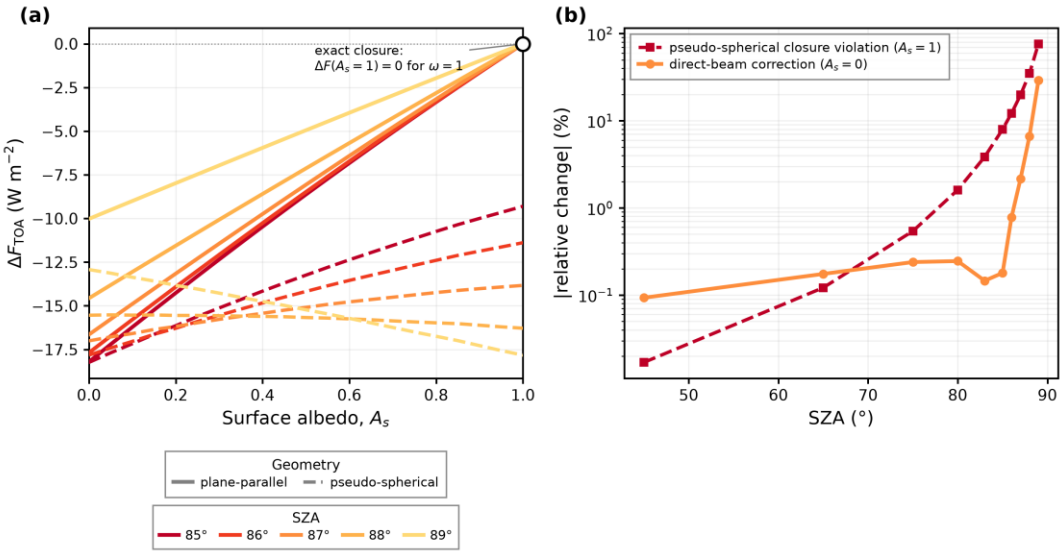


Figure S6. Effect of the pseudo-spherical treatment of the direct beam at large SZA. Panel (a) shows the instantaneous ADRF versus surface albedo at SZA = 85–89°, computed with plane-parallel (solid) and pseudo-spherical (dashed) DISORT (16 streams) for the purely scattering alumina layer of Fig. 1. For ω = 1, the exact ADRF at A_s = 1 is zero (marked). The plane-parallel curves reach this value, but the pseudo-spherical curves do not. The offset, divided by the incident flux, is the violation of the energy balance by the pseudo-spherical calculation. Panel (b) shows the absolute values of the two quantities of Table S3 at each SZA on a logarithmic scale: the relative change in ADRF at A_s = 0 caused by the pseudo-spherical treatment of the direct beam (labeled “direct-beam correction”) and the violation of the energy balance by the pseudo-spherical calculation at A_s = 1 (labeled “closure violation”).

Revised Supplement, Fig. S2 and its caption:

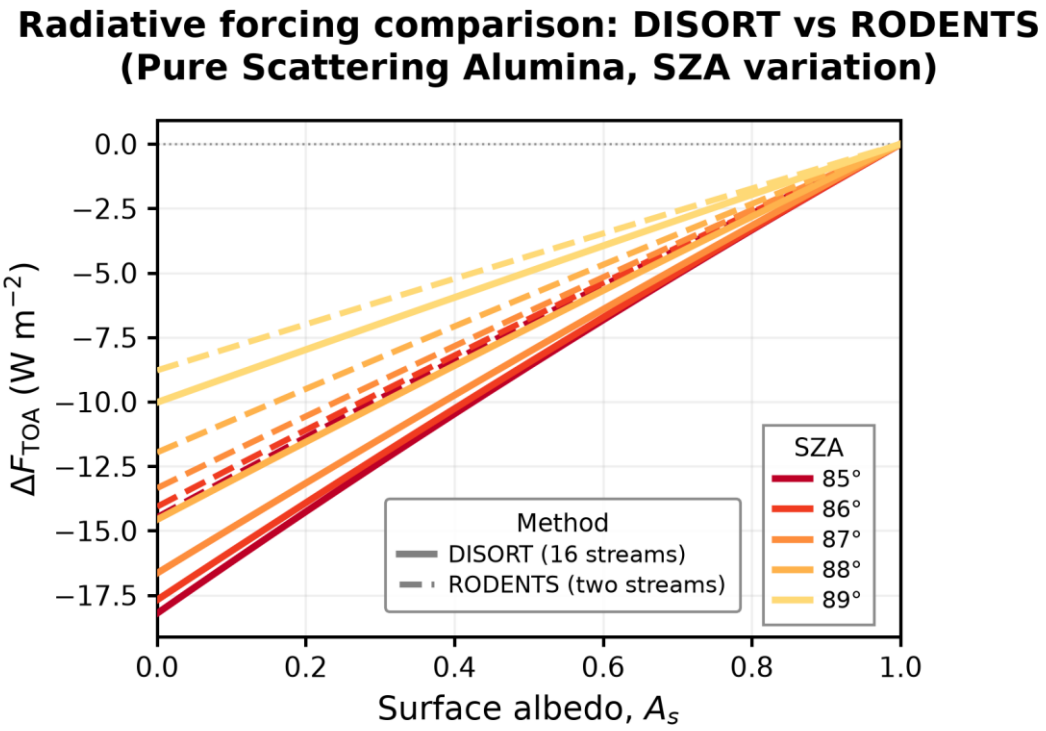


Figure S2. This figure extends Fig. 1 of the main text to the high-SZA range 85–89°. At SZA > 85°, the magnitude of ADRF decreases and approaches zero as SZA approaches 90°. These results are indicative only because the plane-parallel geometry is not reliable for top-of-atmosphere fluxes at SZA > 85° (Sect. S5).

Revised manuscript, lines 503–504:

The Python code and reference output logs for the Monte Carlo geometry checks in Sect. S5 of the Supplement are available on Zenodo (Zhang, 2026; https://doi.org/10.5281/zenodo.23548174).

Specific comments

Specific Comment 1

It would be a good to include the chemical formula for alumina at some point in the manuscript.

We added the formula at the first mention of alumina in the main text.

Revised manuscript, lines 30–33:

Alumina (Al_2O_3), a leading solid-particle candidate, is moreover no longer hypothetical in the stratosphere: in situ measurements show that spacecraft reentry ablation already deposits aluminum-bearing particles in stratospheric aerosol (Murphy et al., 2023), a source projected to grow with rising launch and reentry rates.

Specific Comment 2

L. 84: The abbreviation of ADRF was already introduced before.

We removed the repeated definition; ADRF is now defined once, at its first occurrence in Sect. 1.

Revised manuscript, lines 87–89:

To investigate the sensitivity of ADRF to surface albedo, SZA, and the treatment of multiple scattering, we constructed a plane-parallel, single-layer radiative transfer model representing a homogeneous aerosol slab in the stratosphere above a Lambertian surface.

Specific Comment 3

L. 96: The abbreviation of RTE was already introduced before.

We removed the repeated definition; RTE is now defined once, in Sect. 1.

Revised manuscript, lines 105–108:

The RTE was solved using two methods to evaluate the impact of multiple scattering treatment on ADRF: (1) the Roberts Delta-Eddington Two-Stream solver (RODENTS), representative of the two-stream approximations employed in most general circulation models (Zdunkowski et al., 2007), and (2) the 16-stream DISORT solver (eight streams per hemisphere), which resolves the angular distribution of intensity with higher fidelity (Stamnes et al., 1988).

Specific Comment 4

Figure 1: There is a full stop missing after 'Figure 1' in the figure caption. In addition, after '430 nm' and '18 km to 23 km', there are spaces missing between the numbers and the unit.

We corrected the caption. We also corrected the upper bound of the injection height (18–24 km instead of 18–23 km; Author-initiated correction A1) and the name of the size parameter (median diameter; correction A7).

Revised manuscript, lines 162–165:

Figure 1. Illustration of the sensitivity of ADRF to surface albedo, SZA, and the multiple scattering treatment (DISORT vs. RODENTS) following the injection of pure scattering alumina aerosols. Injected alumina follows the lognormal distribution with median diameter 430 nm, geometric standard deviation 1.5 and number concentration 11.3 cm^{-3}. The injection height is between 18 km and 24 km (stratosphere).

Specific Comment 5

Caption Figure 2: Incorrect panel assignment. Panel (a) shows the diurnal SZA trend (not ARDF).

We corrected the panel assignment.

Revised manuscript, lines 206–208:

> Figure 2a shows the diurnal cycle of SZA for the three latitude bands; Fig. 2b, c and d respectively represent the daily-mean ADRF in the tropics, midlatitudes and polar region on the summer-solstice day in the northern hemisphere.

Specific Comment 6

L. 177: ')' is missing after '(Fig. 2.'.

We added the parenthesis. Because the clause refers to the diurnal cycle of SZA, the reference now points to the panel that shows this cycle (Fig. 2a).

Revised manuscript, lines 216–217:

> This attenuation occurs because the strong negative ADRF at high SZA (morning and evening hours) dominates the time-weighted average, overwhelming the positive forcing that occurs during midday when SZA is low (Fig. 2a).

Specific Comment 7

L. 179: ')' is missing after '(Fig. 2,'.

We added the parenthesis and the panel letter.

Revised manuscript, lines 222–224:

> In the tropics (Fig. 2b) and midlatitudes (Fig. 2c), the daily-mean ADRF from RODENTS remains slightly more negative than that from DISORT, except at the lowest albedos ($A_s \lesssim 0.1$). The difference is pronounced at high A_s values.

Specific Comment 8

L. 183: ')' is missing after '(Fig. 2,'.

We added the parenthesis and the panel letter.

Revised manuscript, lines 226–228:

> In the polar regions (Fig. 2d), the DISORT–RODENTS difference is further reduced, and at low albedos ($A_s < \sim 0.4$) the sign of the bias reverses; RODENTS yields slightly higher (less negative) ADRF than DISORT.

Specific Comment 9

L. 188: '…is non-absorbing…' → are non absorbing

We changed the verb to the plural.

Revised manuscript, lines 231–233:

> Because the aerosol layer and atmosphere medium in our main simulations are non-absorbing, conservation of energy requires that any reduction in TOA reflected flux corresponds to an equivalent increase in shortwave radiation absorbed at the surface.

Specific Comment 10

L. 234: Please use the abbreviation for SZA, as previously introduced.

We made this change and checked the rest of the main text. The opening paragraph of Sect. 4, the Conclusions and the Fig. 4 caption now also use the abbreviation. The spelled-out form remains only in its definition in Sect. 1 and in the abstract.

Revised manuscript, lines 242–243:

We demonstrated in Fig. 1 that even a non-absorbing atmosphere causes positive TOA shortwave radiative forcing over high-albedo surfaces at low SZA.

Revised manuscript, lines 277–279:

However, when the SZA is small, the angular distributions of downwelling and upwelling radiation are fundamentally different, producing different effective reflectances.

Revised manuscript, lines 384–385:

Figure 4. Dependence of the reflectance asymmetry parameter Φ on SZA and surface albedo.

Revised manuscript, lines 404–405:

This study demonstrates that stratospheric aerosol injection using purely scattering particles can produce positive shortwave radiative forcing over high-albedo surfaces at low SZA.

Specific Comment 11

L. 258: Please correct the reference (add the year).

We removed the parenthetical citation instead of adding the year. Zero aerosol absorption is a modeling assumption of this study (Sect. 2.1), whereas measured alumina absorbs weakly (Kapoor et al., 2026).

Revised manuscript, lines 307–308:

Since we assume absorption to be negligible, energy closure gives:

Specific Comment 12

Figure 4: Y-axis labelling: A different symbol to the one used in the text?

The y-axis label of the regenerated Fig. 4 now reads "Reflectance asymmetry parameter, Φ = R↑/R↓", matching the text. The Fig. 4 caption and one sentence in the Conclusions used "reflectance ratio parameter"; both now use the same term (Author-initiated correction A3).

Revised manuscript, Fig. 4 and its caption (lines 384–388):

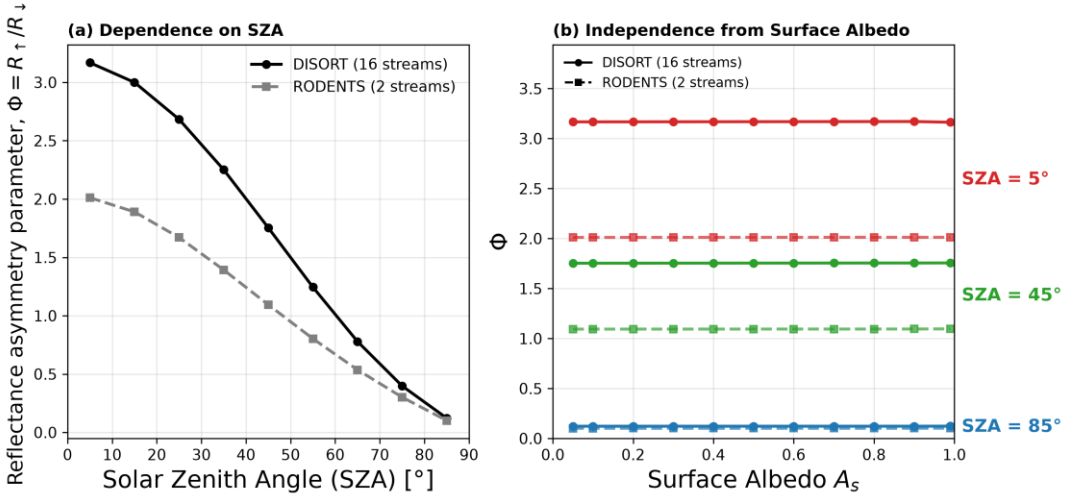


Figure 4. Dependence of the reflectance asymmetry parameter Φ on SZA and surface albedo. (a) Φ as a function of SZA, illustrating the systematic bias between DISORT (solid) and RODENTS (dashed) solvers. (b) Φ as a function of surface albedo (A_s) for three representative SZA values (5°, 45°, 85°). Note that Φ remains constant with respect to A_s, confirming the model prediction that reflectance asymmetry is independent of the underlying surface albedo.

Specific Comment 13

L. 341: Two full stops have been used at the end of the sentence here. Please correct this.

The sentence that ended with two full stops was replaced in response to Comment 2 of Reviewer 2. The new text states the results obtained with a molecular atmosphere.

Revised manuscript, lines 456–458:

With the US standard atmosphere included (Sect. S8), the forcing remains positive over bright surfaces at small SZA and the solver difference persists. The critical surface albedo rises (from 0.32 to 0.44 at SZA = 5°), and the peak forcing decreases (from +3.1 to +2.0 W m^{-2}).

Specific Comment 14

L. 351: 'PyMisScatt' → PyMieScatt?

We corrected the spelling.

Revised manuscript, lines 501–502:

The PyMieScatt Python package (Sumlin et al., 2018) is available for download at https://github.com/bsumlin/PyMieScatt.

Specific Comment 15

L. 352: Please correct the reference.

We corrected the citation.

Revised manuscript, lines 501–502:

> The PyMieScatt Python package (Sumlin et al., 2018) is available for download at https://github.com/bsumlin/PyMieScatt.

Author-initiated corrections

While checking the model configuration for General Comment 1 of Reviewer 1, we compared the source data for every figure with the corresponding model input files. Some submitted figures used settings from an earlier stage of the work: a spectral band of 250–800 nm instead of 250–3000 nm and, for the SZA = 5° and 25° curves of Fig. 1, a Henyey–Greenstein test phase function with g = 0.7 instead of the Mie phase function. We reran all simulations for Figs. 1, 2, 4 and S1–S3 with the configuration stated in Sect. 2 (Mie optical properties from PyMieScatt, 250–3000 nm, DISORT with 16 streams and RODENTS) and replaced these figures. The conclusions are unchanged. The corrected reflectance asymmetry, peak forcing and difference between DISORT and RODENTS are larger. The following numbers in the text changed:

1. Section 3: the maximum instantaneous ADRF at SZA = 5° is +3.1 W m^{-2} at $A_s \approx 0.65$ (previously +2 W m^{-2} at $A_s = 0.6$). The zero crossing at SZA = 5° in Fig. 1 moves from $A_s \approx 0.23$ to $A_s \approx 0.32$. The SZA range in which DISORT gives a higher ADRF than RODENTS now reads 5–65°, at 65° only for $A_s \geq 0.2$ (previously 0–65°).

Revised manuscript, lines 173–176:

> However, at lower SZA (e.g., $\theta < 45°$) the sign of ADRF becomes more complicated: ADRF initially grows (less negative forcing) with increasing A_s, and crosses zero to become positive. It reaches a maximum (e.g., ADRF = +3.1 W m^{-2} at $\theta = 5°$, $A_s \approx 0.65$, using the DISORT solver), and then decreases to zero at $A_s = 1$. Positive ADRF indicates a net reduction in the flux reflected to space despite the aerosol being purely scattering.

Revised manuscript, lines 187–189:

> At SZA values between approximately 5° and 65° (at 65°, only for $A_s \geq 0.2$), DISORT yields higher (more positive) ADRF than RODENTS, meaning that the two-stream approximation underestimates the positive forcing in this regime.

Revised manuscript, Fig. 1 and its caption (lines 162–165):

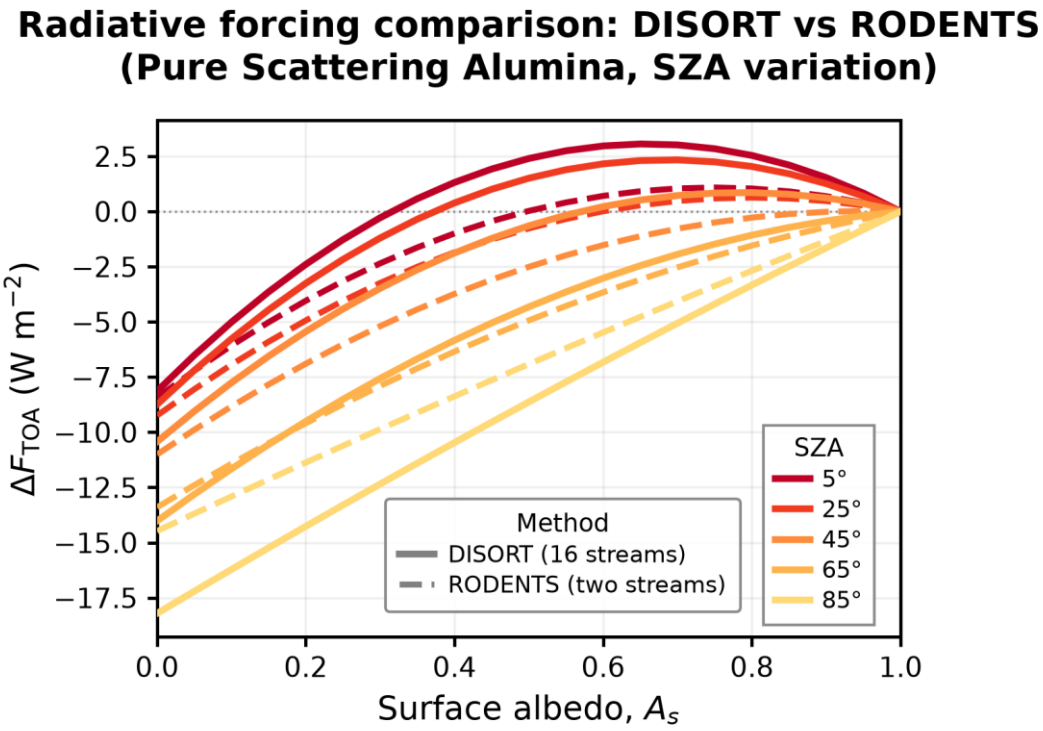


Figure 1. Illustration of the sensitivity of ADRF to surface albedo, SZA, and the multiple scattering treatment (DISORT vs. RODENTS) following the injection of pure scattering alumina aerosols. Injected alumina follows the lognormal distribution with median diameter 430 nm, geometric standard deviation 1.5 and number concentration 11.3 cm^{-3}. The injection height is between 18 km and 24 km (stratosphere).

2. Section 4.4: $\Phi \approx 3.2$ for DISORT at SZA = 5°. The previously quoted value of 2.0 was the RODENTS value, which remains ≈ 2.0. The $\Phi = 1$ crossover is at ≈ 60° for DISORT and at ≈ 48° for RODENTS (previously 55–60° and ≈ 45°).

Revised manuscript, lines 366–373:

Figure 4a shows Φ as a function of SZA for both DISORT and RODENTS. At low SZA, Φ is substantially greater than unity ($\Phi \approx 3.2$ for DISORT and $\Phi \approx 2.0$ for RODENTS at SZA = 5°), confirming that the layer reflects a much larger fraction of diffuse upwelling light than collimated downwelling light. As SZA increases, Φ decreases monotonically. It crosses unity near SZA ≈ 60° for DISORT, as expected from Eq. (15), and near 48° for RODENTS. At larger SZA, Φ falls below unity: R↓ exceeds R↑ (Fig. S3), and the layer reflects the direct beam more strongly than the diffuse upwelling light, consistent with the negative ADRF at high SZA (Figs. 1 and S2).

Revised manuscript, Fig. 4 and its caption (lines 384–388):

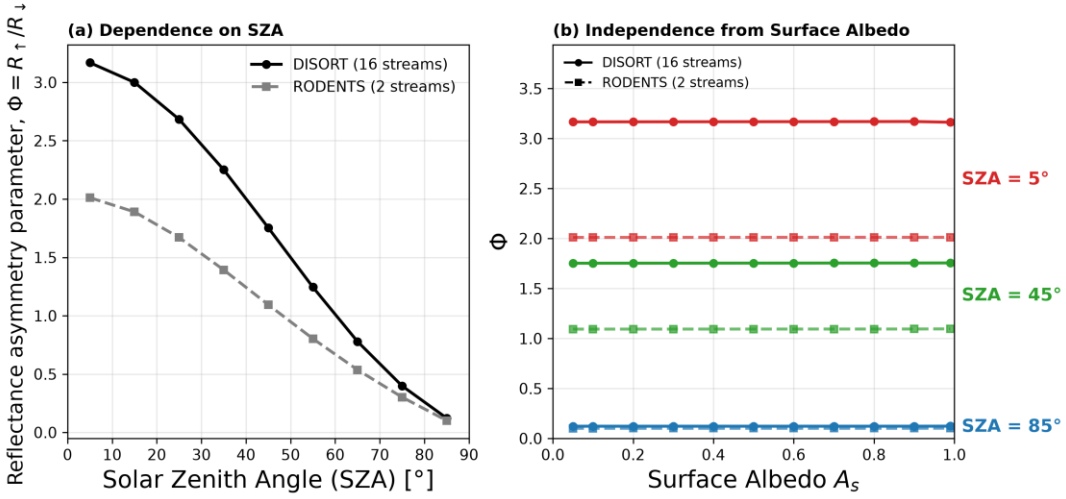


Figure 4. Dependence of the reflectance asymmetry parameter Φ on SZA and surface albedo. (a) Φ as a function of SZA, illustrating the systematic bias between DISORT (solid) and RODENTS (dashed) solvers. (b) Φ as a function of surface albedo (A_s) for three representative SZA values (5°, 45°, 85°). Note that Φ remains constant with respect to A_s, confirming the model prediction that reflectance asymmetry is independent of the underlying surface albedo.

3. Section 3: in the polar panel of Fig. 2, the reversal of the sign of the solver bias extends to $A_s \lesssim 0.4$ (previously ~0.2).

Revised manuscript, lines 226–228:

In the polar regions (Fig. 2d), the DISORT–RODENTS difference is further reduced, and at low albedos (A_s < ~0.4) the sign of the bias reverses; RODENTS yields slightly higher (less negative) ADRF than DISORT.

Revised manuscript, Fig. 2 and its caption (lines 204–211):

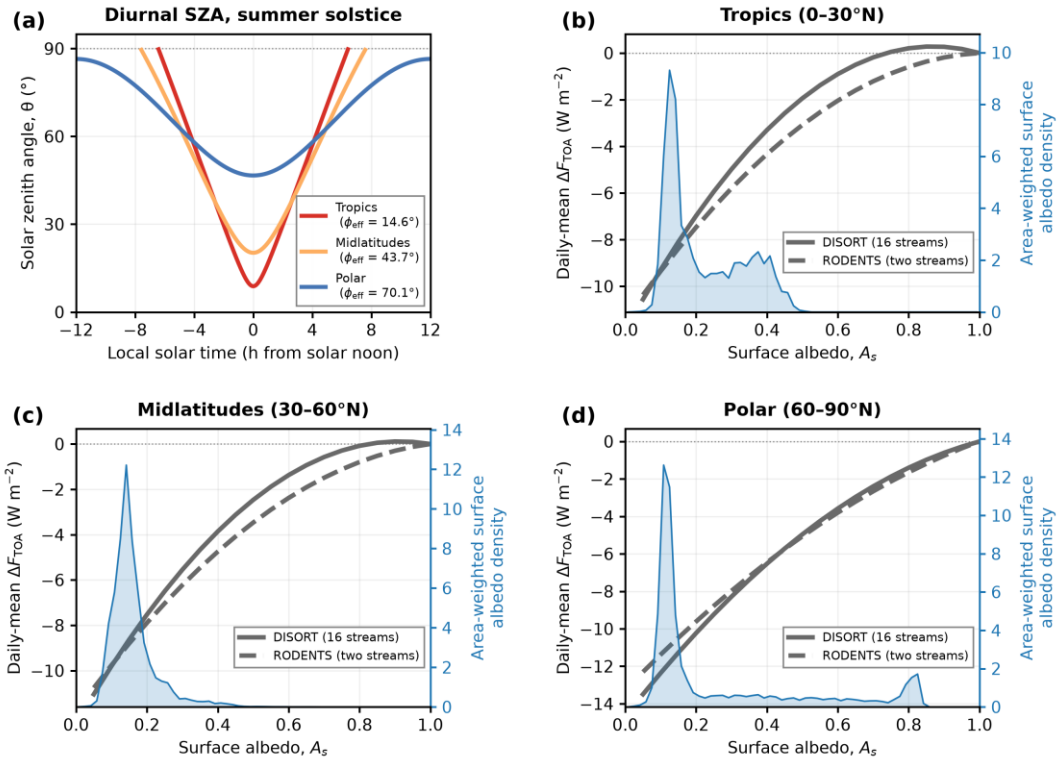


Figure 2. Daily-mean ADRF at the effective latitude of each latitude band, as a function of the prescribed uniform surface albedo A_s. The method for calculating this averaged ADRF is described in Sect. 2.3. Figure 2a shows the diurnal cycle of SZA for the three latitude bands; Fig. 2b, c and d respectively represent the daily-mean ADRF in the tropics, midlatitudes and polar region on the summer-solstice day in the northern hemisphere. The solid lines represent DISORT 16 streams solver and dashed lines represent RODENTS two streams solver. The shaded blue areas represent the area-weighted frequency distributions of the MODIS surface albedo in the corresponding latitude bands (June–August 2025); they are shown for reference and do not enter the averaging.

4. Section 2.1: the number concentration is stated as 11.3 cm^{-3} (previously rounded to 11), and the simulated SZA range is stated as 5–89°.

Revised manuscript, lines 95–98:

We assumed a lognormal particle size distribution with a median diameter of 430 nm, a geometric standard deviation of 1.5, and a number concentration of 11.3 cm^{-3}. These parameters are similar to those used by Dykema et al. (2016) to produce radiative forcing of 1 W m^{-2} with alumina particles.

Revised manuscript, lines 109–111:

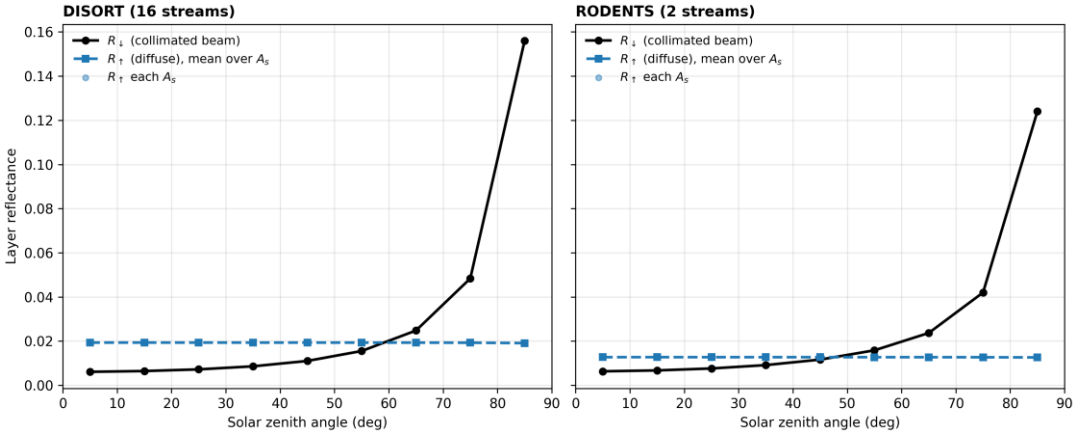
Simulations were performed across surface albedo values from 0 to 1 and SZA values from 5° to 89° to simulate plausible ranges of influence of diurnal and latitudinal changes to radiative forcing.

5. Section 4.4: R↑ is described as independent of surface albedo and constant to within about 1 % across SZA (previously "constant across both").

Revised manuscript, lines 362–364:

> The extracted reflectances are shown separately in Fig. S3: R↓ increases monotonically with SZA, reflecting the lengthening slant path of the collimated beam, whereas R↑ is independent of surface albedo and varies by less than about 1 % across SZA.

Revised Supplement, Fig. S3 and its caption:



> **Figure S3.** Downwelling and upwelling layer reflectances R↓ and R↑ as functions of solar zenith angle, extracted from the same simulations as Fig. 4 via Eqs. (10) and (11), for (a) DISORT (16 streams) and (b) RODENTS (2 streams). R↓ (black circles), the layer reflectance to the collimated solar beam, increases monotonically with SZA as the beam's slant path through the layer ($\propto 1/\cos\theta$) lengthens. R↑ (blue squares), the layer reflectance to the diffuse upwelling field, is shown as the mean over surface albedos $A_s \in [0.3, 0.95]$; light-blue points show the individual estimates extracted independently at each A_s, which coincide at every SZA. R↑ is independent of A_s and varies by less than about 1 % across SZA, consistent with the model assumption that the upwelling field incident on the layer base is isotropic and therefore carries no memory of the solar geometry. Estimates at small A_s are excluded from the mean because Eq. (11) is ill-conditioned as $A_s \to 0$. The SZA-dependence of Φ in Fig. 4a therefore originates entirely in R↓; the crossing R↓ = R↑ marks $\Phi = 1$.

6. Section 3: with the regenerated Fig. 2, the daily-mean ADRF computed with DISORT becomes positive only at $A_s \geq 0.74$ in the tropics and $A_s \geq 0.83$ at midlatitudes, and it remains at or below zero in the polar band (previously "$A_s > \sim 0.8$", with such values described as rare outside polar regions).

Revised manuscript, lines 217–220:

> With DISORT, the daily-mean ADRF becomes positive only at very high surface albedo ($A_s \geq 0.74$ in the tropics and $A_s \geq 0.83$ at midlatitudes), and such values are rare in these bands. In the polar band, the daily-mean ADRF remains at or below zero at every surface albedo.

We also made the following corrections:

A1. The aerosol layer extended from 18 to 24 km in all calculations, rather than 18–23 km as stated in the submitted text. The six 1 km aerosol layers beginning at 18–23 km occupy 18–24 km. We corrected the stated altitude range; the calculated results are unchanged because the simulations already used this configuration.

Revised manuscript, lines 93–94:

> The injected aerosol layer was placed between 18 km and 24 km altitude, corresponding to the lower stratosphere where proposed SAI deployment would occur (Dykema et al., 2016; Weisenstein et al., 2015).

Revised manuscript, lines 162–165:

> **Figure 1.** Illustration of the sensitivity of ADRF to surface albedo, SZA, and the multiple scattering treatment (DISORT vs. RODENTS) following the injection of pure scattering alumina aerosols. Injected alumina follows the lognormal distribution with median diameter 430 nm, geometric standard deviation 1.5 and number concentration 11.3 cm^{-3}. The injection height is between 18 km and 24 km (stratosphere).

A2. We added the missing space after "June–August 2025." in Sect. 3 (the submitted text read "2025.In").

Revised manuscript, lines 225–226:

> Surface albedo distributions were derived from the MODIS MCD43 BRDF/Albedo product (Schaaf and Wang, 2021), averaged over June–August 2025.

A3. The Fig. 4 caption and one sentence in the Conclusions used "reflectance ratio parameter"; both now read "reflectance asymmetry parameter", the term used throughout the text.

Revised manuscript, lines 384–388:

> **Figure 4.** Dependence of the reflectance asymmetry parameter Φ on SZA and surface albedo. (a) Φ as a function of SZA, illustrating the systematic bias between DISORT (solid) and RODENTS (dashed) solvers. (b) Φ as a function of surface albedo (A_s) for three representative SZA values (5°, 45°, 85°). Note that Φ remains constant with respect to A_s, confirming the model prediction that reflectance asymmetry is independent of the underlying surface albedo.

Revised manuscript, lines 415–417:

> We defined a reflectance asymmetry parameter $\Phi = R\uparrow/R\downarrow$ that quantifies this asymmetry and showed analytically that, at fixed R↓, increasing Φ reduces the TOA reflected flux for $0 < A_s < 1$ (Eq. 9).

A4. The Danabasoglu et al. (2020) entry now gives the full list of 43 authors, as ACP requires complete author lists.

Revised manuscript, reference list (lines 536–542):

> Danabasoglu, G., Lamarque, J.-F., Bacmeister, J., Bailey, D. A., DuVivier, A. K., Edwards, J., Emmons, L. K., Fasullo, J., Garcia, R., Gettelman, A., Hannay, C., Holland, M. M.,

Large, W. G., Lauritzen, P. H., Lawrence, D. M., Lenaerts, J. T. M., Lindsay, K., Lipscomb, W. H., Mills, M. J., Neale, R., Oleson, K. W., Otto-Bliesner, B., Phillips, A. S., Sacks, W., Tilmes, S., van Kampenhout, L., Vertenstein, M., Bertini, A., Dennis, J., Deser, C., Fischer, C., Fox-Kemper, B., Kay, J. E., Kinnison, D., Kushner, P. J., Larson, V. E., Long, M. C., Mickelson, S., Moore, J. K., Nienhouse, E., Polvani, L., Rasch, P. J., and Strand, W. G.: The Community Earth System Model Version 2 (CESM2), J. Adv. Model. Earth Sy., 12, e2019MS001916, https://doi.org/10.1029/2019MS001916, 2020.

A5. We added the missing volume number of Kumar et al. (2026) (J. Aerosol Sci., 194, 106767).

Revised manuscript, reference list (lines 573–574):

Kumar, J., Jung, G. Y., Kapoor, T. S., Mishra, R., and Chakrabarty, R. K.: Strong light absorption by sp2 hybridized carbon impurities in diamond dust, J. Aerosol Sci., 194, 106767, https://doi.org/10.1016/j.jaerosci.2026.106767, 2026.

A6. The daily SZA weighting for Fig. 2 had been computed for 1 June, whereas the caption states the summer solstice. We regenerated the figure for 21 June. The date change alone has a minor effect on the figure and affects no conclusion. The daily-mean ADRF in Fig. 2b and c is larger in magnitude than in the submitted figure because these panels had been computed for 250–800 nm, whereas Fig. 2d already used 250–3000 nm.

A7. Section 2.1 and the captions of Figs. 1 and S1 called the 430 nm parameter of the lognormal distribution the "mean diameter". This parameter is the median (geometric mean) diameter of the number distribution, and the text now reads "median diameter".

Revised manuscript, lines 95–98:

We assumed a lognormal particle size distribution with a median diameter of 430 nm, a geometric standard deviation of 1.5, and a number concentration of 11.3 cm^{-3}. These parameters are similar to those used by Dykema et al. (2016) to produce radiative forcing of 1 W m^{-2} with alumina particles.

Revised Supplement, caption of Fig. S1:

Figure S1. It illustrates the sensitivity of ADRF to surface albedo, SZA, and the multiple scattering treatment (DISORT vs. RODENTS) following the injection of alumina aerosols with imaginary part from Kapoor et al. (2026). Injected alumina follows the lognormal distribution with median diameter 430 nm, geometric standard deviation 1.5 and number concentration 11.3 cm^{-3}. The injection height is between 18 km and 24 km (stratosphere).

A8. The submitted text cited Maloney et al. (2025) and Robock et al. (2008), which were missing from the reference list; both entries have been added.

Revised manuscript, reference list (lines 577–579 and 602–603):

Maloney, C. M., Portmann, R. W., Ross, M. N., and Rosenlof, K. H.: Investigating the potential atmospheric accumulation and radiative impact of the coming increase in satellite reentry frequency, J. Geophys. Res.-Atmos., 130, e2024JD042442, https://doi.org/10.1029/2024JD042442, 2025.

Robock, A., Oman, L., and Stenchikov, G. L.: Regional climate responses to geoengineering with tropical and Arctic SO_2 injections, J. Geophys. Res., 113, D16101, https://doi.org/10.1029/2008JD010050, 2008.

A9. Abstract: "bright surfaces such as snow and ice" now reads "bright surfaces such as snow and desert". The phrase "through the layer and is preferentially backscattered to the surface" now reads "through the aerosol layer and is preferentially backscattered to the ground". The phrase "may underestimate the localized climatic risks" now reads "may underestimate localized climatic risks".

Revised manuscript, lines 11–12:

This study investigates the counter-intuitive positive shortwave radiative forcing induced by purely scattering aerosols over bright surfaces such as snow and desert.

Revised manuscript, lines 17–19:

We introduce the reflectance asymmetry parameter (Φ) to quantify this asymmetry: diffuse upwelling light encounters a longer optical path through the aerosol layer and is preferentially backscattered to the ground.

Revised manuscript, lines 20–22:

These findings suggest that current assessments may underestimate localized climatic risks of SAI and extend to any optically thin scattering layer over bright surfaces – including the growing burden of reentry-derived alumina.

A10. Supplement, Eq. (S7): we corrected a typographical error in the range of t_{hours} ([−12.12) → [−12, 12)).

Revised Supplement, Sect. S2, Eq. (S7):

$$h(t) = 15^{\circ} \cdot t_{hours},\ t_{hours} \in [-12, 12) \qquad \text{(S7)}$$

A11. Supplement, Sects. S1 and S2: we corrected three typographical errors in the equations. In Eq. (S2), the sum now runs over the moment index l and includes the factor (2l + 1)/2; P_l now takes $\mu_i = \cos\theta_i$ instead of θ_i. In Eq. (S3), the trapezoidal sum now uses $(\mu_i - \mu_{i+1})$ because μ_i decreases with i. In Sect. S2, λ in the area element is the longitude, not the latitude.

Revised Supplement, Sect. S1, Eq. (S2):

$$P_{\text{Mie}}(\theta_i) \approx \sum_{l=0}^{32} \frac{2l+1}{2} k_l P_l(\mu_i), \quad \text{with} \quad \mu_i = \cos\theta_i \qquad \text{(S2)}$$

Revised Supplement, Sect. S1, Eq. (S3):

$$k_l = \int_{-1}^{1} P_{\text{Mie}}(\mu) P_l(\mu) \mathrm{d}\mu \approx \sum_{i=0}^{N-1} \frac{1}{2} [P_{\text{Mie}}(\mu_i) P_l(\mu_i) + P_{\text{Mie}}(\mu_{i+1}) P_l(\mu_{i+1})](\mu_i - \mu_{i+1}) \qquad \text{(S3)}$$

Revised Supplement, Sect. S2, text after Eq. (S6):

One can treat ϕ_{eff} as the cosine-area-weighted mean latitude (It's a standard way in climate data averaging because the surface-area element on a sphere is $dA = R^2 \cos\phi\, d\phi\, d\lambda$, λ is longitude).

A12. We corrected "Hartmann et al., 2016" to "Hartmann, 2016" because the book has a single author. We also replaced the reference to the preprint of Kapoor et al. (2026) with the published article in Geophysical Research Letters, in both the manuscript and the Supplement.

Revised manuscript, lines 473–474:

> Clouds possess high albedo (0.4–0.9 depending on thickness, water content, and type) (Hartmann, 2016) and reside at altitudes (2–12 km) below the modeled SAI injection height.

Revised manuscript, reference list (lines 568–572), and revised Supplement, reference list:

> Kapoor, T. S., Upadhyay, P., Huang, J., Ren, G., Cavin, J., Mitroo, D., Vattioni, S., Dykema, J., Sedlacek, J., Kumar, J., Hachtel, J. A., Xu, L., Mishra, R., and Chakrabarty, R. K.: Unveiling the shortwave absorption spectra of alumina aerosols: radiative implications for solar radiation modification, Geophys. Res. Lett., 53, e2026GL121668, https://doi.org/10.1029/2026GL121668, 2026.

A13. We corrected three statements that did not match the equations or figures. Section 2.1 described the ADRF as the change in net upward flux, whereas its defining equation gives the change in net downward flux. Section 4.3 stated that increasing Φ lowers the radiative forcing, whereas Eq. (9) shows that it raises the ADRF. The opening of Sect. 4 cited Fig. 2b for the lower SZA at low latitudes, which is shown in Fig. 2a. The sentence of the Conclusions quoted under A3 now also states that Eq. (9) applies at fixed $R\downarrow$ and for $0 < A_s < 1$.

Revised manuscript, lines 116–117:

> The ADRF is then defined as the change in net downward shortwave flux at the TOA due to the presence of the aerosol layer:

Revised manuscript, line 318:

> Thus, increasing Φ lowers E (and raises the ADRF) for $0 < A_s < 1$.

Revised manuscript, lines 247–249:

> Regions where low SZA coincides with high surface albedo – such as low-latitude deserts, salt flats, and snow-covered mountains – are therefore susceptible to this mechanism (Fig. 2a).

References

Brownlee, D. E., Ferry, G. V., and Tomandl, D.: Stratospheric aluminum oxide, Science, 191, 1270–1271, https://doi.org/10.1126/science.191.4233.1270, 1976.

Danabasoglu, G., Lamarque, J.-F., Bacmeister, J., Bailey, D. A., DuVivier, A. K., Edwards, J., Emmons, L. K., Fasullo, J., Garcia, R., Gettelman, A., Hannay, C., Holland, M. M., Large, W. G., Lauritzen, P. H., Lawrence, D. M., Lenaerts, J. T. M., Lindsay, K., Lipscomb, W. H., Mills, M. J., Neale, R., Oleson, K. W., Otto-Bliesner, B., Phillips, A. S., Sacks, W., Tilmes, S., van Kampenhout, L., Vertenstein, M., Bertini, A., Dennis, J., Deser, C., Fischer, C., Fox-Kemper, B., Kay, J. E., Kinnison, D., Kushner, P. J., Larson, V. E., Long, M. C., Mickelson, S., Moore, J. K., Nienhouse, E., Polvani, L., Rasch, P. J., and Strand, W. G.: The

Community Earth System Model Version 2 (CESM2), J. Adv. Model. Earth Sy., 12, e2019MS001916, https://doi.org/10.1029/2019MS001916, 2020.

Dumont, M., Brissaud, O., Picard, G., Schmitt, B., Gallet, J.-C., and Arnaud, Y.: High-accuracy measurements of snow Bidirectional Reflectance Distribution Function at visible and NIR wavelengths – comparison with modelling results, Atmos. Chem. Phys., 10, 2507–2520, https://doi.org/10.5194/acp-10-2507-2010, 2010.

Dykema, J. A., Keith, D. W., and Keutsch, F. N.: Improved aerosol radiative properties as a foundation for solar geoengineering risk assessment, Geophys. Res. Lett., 43, 7758–7766, https://doi.org/10.1002/2016GL069258, 2016.

Emde, C., Buras-Schnell, R., Kylling, A., Mayer, B., Gasteiger, J., Hamann, U., Kylling, J., Richter, B., Pause, C., Dowling, T., and Bugliaro, L.: The libRadtran software package for radiative transfer calculations (version 2.0.1), Geosci. Model Dev., 9, 1647–1672, https://doi.org/10.5194/gmd-9-1647-2016, 2016.

Ferreira, J. P., Huang, Z., Nomura, K., and Wang, J.: Potential ozone depletion from satellite demise during atmospheric reentry in the era of mega-constellations, Geophys. Res. Lett., 51, e2024GL109280, https://doi.org/10.1029/2024GL109280, 2024.

Hansen, J. E.: Multiple scattering of polarized light in planetary atmospheres. Part II. Sunlight reflected by terrestrial water clouds, J. Atmos. Sci., 28, 1400–1426, https://doi.org/10.1175/1520-0469(1971)028<1400:MSOPLI>2.0.CO;2, 1971.

Hartmann, D. L.: Global Physical Climatology, 2nd edn., Elsevier, Amsterdam, the Netherlands, https://doi.org/10.1016/C2009-0-00030-0, 2016.

Hudson, S. R., Warren, S. G., Brandt, R. E., Grenfell, T. C., and Six, D.: Spectral bidirectional reflectance of Antarctic snow: measurements and parameterization, J. Geophys. Res., 111, D18106, https://doi.org/10.1029/2006JD007290, 2006.

Kapoor, T. S., Upadhyay, P., Huang, J., Ren, G., Cavin, J., Mitroo, D., Vattioni, S., Dykema, J., Sedlacek, J., Kumar, J., Hachtel, J. A., Xu, L., Mishra, R., and Chakrabarty, R. K.: Unveiling the shortwave absorption spectra of alumina aerosols: radiative implications for solar radiation modification, Geophys. Res. Lett., 53, e2026GL121668, https://doi.org/10.1029/2026GL121668, 2026.

Kumar, J., Jung, G. Y., Kapoor, T. S., Mishra, R., and Chakrabarty, R. K.: Strong light absorption by sp2 hybridized carbon impurities in diamond dust, J. Aerosol Sci., 194, 106767, https://doi.org/10.1016/j.jaerosci.2026.106767, 2026.

Lacis, A. A., Chowdhary, J., Mishchenko, M. I., and Cairns, B.: Modeling errors in diffuse-sky radiation: vector vs. scalar treatment, Geophys. Res. Lett., 25, 135–138, https://doi.org/10.1029/97GL03613, 1998.

Maloney, C. M., Portmann, R. W., Ross, M. N., and Rosenlof, K. H.: Investigating the potential atmospheric accumulation and radiative impact of the coming increase in satellite reentry frequency, J. Geophys. Res.-Atmos., 130, e2024JD042442, https://doi.org/10.1029/2024JD042442, 2025.

Marchuk, G. I., Mikhailov, G. A., Nazaraliev, M. A., Darbinjan, R. A., Kargin, B. A., and Elepov, B. S.: The Monte Carlo Methods in Atmospheric Optics, Springer Series in Optical

Sciences, 12, Springer, Berlin, Heidelberg, https://doi.org/10.1007/978-3-540-35237-2, 1980.

Mayer, B.: Radiative transfer in the cloudy atmosphere, EPJ Web Conf., 1, 75–99, https://doi.org/10.1140/epjconf/e2009-00912-1, 2009.

Mishchenko, M. I., Lacis, A. A., and Travis, L. D.: Errors induced by the neglect of polarization in radiance calculations for Rayleigh-scattering atmospheres, J. Quant. Spectrosc. Ra., 51, 491–510, https://doi.org/10.1016/0022-4073(94)90149-X, 1994.

Mishchenko, M. I., Travis, L. D., Kahn, R. A., and West, R. A.: Modeling phase functions for dustlike tropospheric aerosols using a shape mixture of randomly oriented polydisperse spheroids, J. Geophys. Res., 102, 16831–16847, https://doi.org/10.1029/96JD02110, 1997.

Murphy, D. M., Abou-Ghanem, M., Cziczo, D. J., Froyd, K. D., Jacquot, J., Lawler, M. J., Maloney, C., Plane, J. M. C., Ross, M. N., Schill, G. P., and Shen, X.: Metals from spacecraft reentry in stratospheric aerosol particles, P. Natl. Acad. Sci. USA, 120, e2313374120, https://doi.org/10.1073/pnas.2313374120, 2023.

Prahl, S.: miepython, version 3.3.0, GitHub [code], https://github.com/scottprahl/miepython/releases/tag/3.3.0, 2026.

Robock, A., Oman, L., and Stenchikov, G. L.: Regional climate responses to geoengineering with tropical and Arctic SO_2 injections, J. Geophys. Res., 113, D16101, https://doi.org/10.1029/2008JD010050, 2008.

Schaaf, C. and Wang, Z.: MODIS/Terra+Aqua BRDF/Albedo Albedo Daily L3 Global 0.05Deg CMG V061, NASA Land Processes Distributed Active Archive Center [data set], https://doi.org/10.5067/MODIS/MCD43C3.061, 2021.

Stamnes, K., Tsay, S.-C., Wiscombe, W., and Jayaweera, K.: Numerically stable algorithm for discrete-ordinate-method radiative transfer in multiple scattering and emitting layered media, Appl. Optics, 27, 2502–2509, https://doi.org/10.1364/AO.27.002502, 1988.

Stamnes, K., Thomas, G. E., and Stamnes, J. J.: Radiative Transfer in the Atmosphere and Ocean, 2nd edn., Cambridge University Press, Cambridge, https://doi.org/10.1017/9781316148549, 2017.

Sumlin, B. J., Heinson, W. R., and Chakrabarty, R. K.: Retrieving the aerosol complex refractive index using PyMieScatt: a Mie computational package with visualization capabilities, J. Quant. Spectrosc. Ra., 205, 127–134, https://doi.org/10.1016/j.jqsrt.2017.10.012, 2018.

Tropf, W. J. and Thomas, M. E.: Aluminum oxide (Al2O3) revisited, in: Handbook of Optical Constants of Solids, edited by: Palik, E. D., Academic Press, 653–682, https://doi.org/10.1016/B978-012544415-6.50124-2, 1997.

Vattioni, S., Weber, R., Feinberg, A., Stenke, A., Dykema, J. A., Luo, B., Kelesidis, G. A., Bruun, C. A., Sukhodolov, T., Keutsch, F. N., Peter, T., and Chiodo, G.: A fully coupled solid-particle microphysics scheme for stratospheric aerosol injections within the aerosol–chemistry–climate model SOCOL-AERv2, Geosci. Model Dev., 17, 7767–7793, https://doi.org/10.5194/gmd-17-7767-2024, 2024.

Warren, S. G.: Optical properties of snow, Rev. Geophys., 20, 67–89, https://doi.org/10.1029/RG020i001p00067, 1982.

Weisenstein, D. K., Keith, D. W., and Dykema, J. A.: Solar geoengineering using solid aerosol in the stratosphere, Atmos. Chem. Phys., 15, 11835–11859, https://doi.org/10.5194/acp-15-11835-2015, 2015.

Wiscombe, W. J.: The delta-M method: rapid yet accurate radiative flux calculations for strongly asymmetric phase functions, J. Atmos. Sci., 34, 1408–1422, https://doi.org/10.1175/1520-0469(1977)034<1408:TDMRYA>2.0.CO;2, 1977.

Zdunkowski, W., Trautmann, T., and Bott, A.: Radiation in the Atmosphere: A Course in Theoretical Meteorology, Cambridge University Press, Cambridge, UK, 2007.

Zhang, L.: Monte Carlo geometry checks for “Purely light-scattering aerosols could induce positive shortwave radiative forcing over high-albedo surfaces”, version 1.0.0, Zenodo [code], https://doi.org/10.5281/zenodo.23548174, 2026.